

Supporting Information for

Ultra-broadband plasmon driving selective photoreforming of methanol under ambient conditions

Nasir Uddin^{a#}, Zhehao Sun^{a,b#}, Julien Langley^a, Dr. Haijao Lu^a, Dr. Pengfei Cao^{c*}, Ary Wibowo^d, Dr. Xinmao Yin^{e,f}, Dr. Chi Sin Tang^g, Dr. Hieu T. Nguyen^d, Dr. Jack Evans^a, Xinzhe Li^h, Xiaoliang Zhangⁱ, Dr. Marc Heggen^c, Dr. Rafal E. Dunin Borkowski^c, Andrew T.S. Wee^f, Dr. Haitao Zhao^{b*}, Dr. Nicholas Cox^a & Dr. Zongyou Yin^{a*}

^aResearch School of Chemistry, Australian National University, ACT 2601, Australia; ^bMaterials Interfaces Center, Shenzhen Institute of Advanced Technology, Chinese Academy of Sciences, Shenzhen 518055, Guangdong, PR China; ^cErnst Ruska-Centre for Microscopy and Spectroscopy with Electrons, Forschungszentrum Jülich GmbH, 52428 Jülich, Germany; ^dResearch School of Electrical, Energy and Materials Engineering, Australian National University, ACT 2601, Australia; ^eShanghai Key Laboratory of High Temperature Superconductors, Physics Department, Shanghai University, Shanghai, 200444, China; ^fDepartment of Physics, Faculty of Science, National University of Singapore, Singapore 117542, Singapore; ^gSingapore Synchrotron Light Source (SSLS), National University of Singapore, Singapore 117603; ^hState Key Laboratory of Multiphase Flow in Power Engineering, Xi'an Jiaotong University, Xi'an 710049, Shaanxi, P.R. China and ⁱInstitute of Energy and Environmental Engineering, School of Energy and Power Engineering, Dalian University of Technology, Dalian 116024, PR China.

*To whom correspondence may be addressed. **Email:** p.cao@fz-juelich.de; ht.zhao@siat.ac.cn; zongyou.yin@anu.edu.au

This PDF file includes:

Supplementary text
Figures S1 to S38
Tables S1 to S7
SI References

Supplementary Text

Preparation and Optimization of photocatalysts for CH₃OH dehydrogenation

Catalysts preparation. The W-C phase diagram suggests that the formation of WC is thermodynamically favoured between 300 to 1200 °C (1). To form WC, the relative amount of carbon precursor to tungsten precursor is needed to be at 50% based on the phase diagram (1) and employed the carburization process at high temperature in a vacuum or hydrogen atmosphere. Under vacuum, carbon diffusion is limited to very short distances, suggesting WC only forms when the solid carbon source directly interacts with tungsten (2). Conversely, a homogeneous distribution of carbon can be possible during carburization in hydrogen atmosphere (2). Under a hydrogen atmosphere, carbon travel in the form of hydrocarbons over a distance from several millimetres to centimetres (2). Within this work, we used a complex mixture of tungstic acid (H₂WO₄), urea and ethanol in a H₂/Ar gas mixture atmosphere under vacuum conditions. The carburization was carried out for 3 hours at 850 °C with slow ramping of 2 °C/min. Here urea functions as a carbon source for WC. Due to high temperature decomposition, urea can produce various gaseous products: NH₃, CO₂ and CO gases (3). Ethanol serves as a complexing agent and remain at trace level which eliminates from reaction tubular furnace as temperature rises. With continuous H₂/Ar gases mixture, much of the tungsten precursor reduces into metallic W, and carbon contents decrease due to the produced gases (NH₃, CO₂, CO, etc.) (4) from urea has more available time to escape from the outlet of the tubular furnace. Once the temperature reaches at 850 °C (where it is held for 3 hours) the formed gases are more available to metallic W, which may react with solid carbon to form WC. In this way, we synthesized WC/W nanoparticles (NPs). Moreover, the formation of solid carbon from urea at hydrogen atmosphere (5, 6) can induce epitaxial growth of WC on W (7-11). A similar heteroepitaxial growth of WC on W at hydrogen and methane gas mixture environment can be found elsewhere (12). To form the Cu-WC/W composite, we add different weight percentage of Cu source to tungsten precursor complex above following the co-reduction process. At the same time, the formed carbon contents are reduced by reaction with W to form WC, while some reacted with Cu. Note that there is no chemical bonding between Cu and W, signalling that Cu exist as an individual entity on the tungsten skeleton. We introduced other non-noble metals such as Ni, Mg, Ca, and Zr to the above tungsten complex following the same thermal treatment process.

Effects of Cu precursor loading on H₂ production. We prepared four different Cu-WC/W NPs by utilizing 1, 2, 4, and 6 weight percentage of Cu precursor into tungstic acid complex. Once prepared, we tested the H₂ production from pure CH₃OH dehydrogenation using AM 1.5 G simulated light conditions at ambient conditions. After 2 hours of continuous illumination, we observed the hydrogen production efficiency was higher for 2% Cu loading (2176.66 μmole.g⁻¹.h⁻¹) as compared with other studied catalysts as shown in Fig. S1. Additionally, the H₂ formation efficiency was up by almost a factor of 14 for 2% Cu-WC/W NPs compared to bare WC/W NPs (156.83 μmole.g⁻¹.h⁻¹). Note the performance of both of 4 and 6% samples was lower (1310, and 933.71 μmole.g⁻¹.h⁻¹, respectively) than 2% Cu-WC/W NPs but higher than 1% Cu-WC/W NPs sample (620 μmole.g⁻¹.h⁻¹). The sharp maximum rate of 2% Cu-WC/W NPs was associated with the nature of the active site for the reaction (it necessitates the presence of both Cu and WC/W NPs surface) which occurs at the heterointerface where all the feeding components in the reactions, for example, light-excited electrons and adsorbed CH₃OH can be brought together (13). The loss in activity of both of 4 and 6% Cu-WC/W NPs samples indicates further loadings of Cu source, might not improve the H₂ production from pure CH₃OH whereas a similar observation was also made for 1% Cu-WC/W NPs. This might be related to the fact that at higher loadings of Cu NPs, there is reduced reactive area from WC remaining to be exposed to reactants. This is a kind of shadowing of the photoactive support by the Cu NPs, resulting in reduced H₂ production. Similar observations were reported for Au (14), Pd (15) and Pt (16) NPs loadings on TiO₂ materials in H₂ production from photocatalytic CH₃OH steam reforming processes. However, we describe the characterization and optical properties of 2% Cu-WC/W NPs sample elaborately within this study alongside 1% Cu-WC/W NPs and 4% Cu-WC/W NPs samples where appropriate.

Effects of non-noble metals incorporation on H₂ production. Stimulated by higher plasmonic photoactivity of 2% Cu-WC/W NPs from methanol decomposition, we took further steps to check whether Cu-like non-noble metals incorporation to WC/W NPs could provide more H₂ efficiency under AM 1.5 G simulated conditions. As displayed in Fig. S2, the H₂ efficiency magnitude of 2% Cu-WC/W NPs was superior compared to other non-noble based metals-WC/W NPs. This could be related to the

fact that other noble free metals such as Ni, Mg, Ca, and Zr introduction to WC/W NPs might alter the surface of WC/W NPs, possibly with formation of oxides that were not identifiable in the 2% Cu-WC/W NPs. Note that the photocatalytic H₂ formation over bare Cu NPs is deemed to be very low which could be associated with poor dispersion of Cu NPs in CH₃OH solution. This is likely because Cu NPs are highly agglomerated and hence have low solubility in CH₃OH solution. However, agglomerated NPs are reasoned to be effective in increasing the absorption range of Cu NPs because the agglomerations increase the scattering ability of NPs (17). A contrasting observation was made for Cu-WC/W hybrid nanostructure in CH₃OH solution where the composite is easily dissolved in the methanol, resulting in outstanding photocatalytic performance. This is probably linked to the fact that the distribution of Cu particles on WC/W is at low density

Effects of illuminated energy on H₂ production. As noticed from Fig. S3, the H₂ production efficiency is far better under AM 1.5 G simulated light illumination, reaching to 2176.66 $\mu\text{mole}\cdot\text{g}^{-1}\cdot\text{h}^{-1}$ and drops by nearly 2 fold under 420 nm illumination. At 700 and 800 nm, the H₂ efficiency never approached the value observed with AM 1.5 G simulated light irradiance.

XRD analysis. Fig. S4 shows the X-ray diffraction (XRD) pattern for in-situ prepared WC/W sample assignable to elemental W having the body-centered cubic (bcc) structure with multiple peaks at $2\theta = 40.35, 58.37, \text{ and } 73.35^\circ$, corresponding to (011), (002), and (112) plane, respectively (ICSD # 653433); whereas WC shows no visible peaks implying that WC might have a crystalline aspect with short-range order. After the introduction of bare Cu precursor, the XRD pattern of WC/W exhibited three additional peaks, maintaining the peaks related to WC/W while three peaks could be assigned to the (111), (002), and (022) planes of face-centered cubic (fcc) elemental Cu phases located at $2\theta = 43.52, 50.56, \text{ and } 74.28^\circ$, respectively (18, 19). No other peaks were identified, indicating that the in-situ synthesised WC/W nanoparticles (NPs) is free from other impurities. Traditionally, when carbide materials prepared under a reducing hydrogen atmosphere above 800 °C in presence of excessive gaseous carbon precursors, there is a possibility of coke formation on WC surface which can be detrimental towards catalytic activity (20, 21). Nevertheless, the synthetic approach within this study is selectively engineered by limiting the carbon precursor volume which permits the formation of only WC besides elemental W and thus avoiding coking formation.

Complex refractive index and dielectric properties analysis. Figs. S13-14 show the complex refractive index and extinction co-efficient of Cu and WC samples, respectively. The refractive index (n) is the measure of the reduction in the rate of the speed of light in the medium (22) whereas extinction co-efficient (k) is the measure of how fast light energy is lost in the materials. The values of n increases with wavelengths whereas k follows declining characteristics from 400 nm, reaching to almost zero value at near infrared (NIR) region for Cu sample (Fig. S13). With increasing n values, the k values of WC sample (Fig. S14) against wavelength show that WC could harvest visible frequencies starting at 400 nm to the entire NIR region due to the decrease of k value. Parallel observation was marked for metallic W which reveals poor solar light harvesting capacity (both n and k values of W is higher than bare Cu and WC samples) as shown in Fig. S15. It is explicitly evident that bare Cu NPs sample, with lower n and k than WC and W, show the improved light harvesting features for methanol dehydrogenation reaction.

Solar to Hydrogen conversion efficiency. The solar to hydrogen conversion efficiency can be defined as: $\text{STH} = (\text{Power}_{\text{output}}/\text{Power}_{\text{input}}) \times 100\%$

where $\text{Power}_{\text{output}}$ is equal to the multiplication of hydrogen production per second and the free energy required (23) to produce one mole hydrogen from CH₃OH dehydrogenation which was determined to be $\{(8.70 \times 10^{-6}/3600) \times 92.7 \times 10^3\} \approx 2.240 \times 10^{-4} \text{ J/s}$. The $\text{Power}_{\text{input}}$ is equal to the multiplication of power of illumination and the illuminated area which was calculated to be $\{(0.942 \times 10^{-3}) \times 10\} = 9.42 \times 10^{-3} \text{ J/s}$. Based on the above definition, the STH was determined to be $(2.240 \times 10^{-4} \text{ J/s} / 9.42 \times 10^{-3} \text{ J/s}) \times 100\% \approx 2.40 \%$.

Calculation of quantum efficiency. The sample solution was illuminated by a 300 W Xe light source passed through an AM 1.5 G filter, which has an average wavelength of about 550 nm. The irradiated sample solution area was 10 cm² and the average intensity of irradiation was measured using a digital photoradiometer. Based on hydrogen reduction reaction ($2\text{H}^+ + 2\text{e}^- \rightarrow \text{H}_2$), two electrons are needed to generate one hydrogen molecule. Apparent quantum efficiency (AQE) was calculated at $\lambda = 550$ nm for 2% Cu-WC/W NPs catalysts in pure methanol by combining the molar amount of H₂ and the number of absorbed photons as shown: The amount of hydrogen molecules produced per second (N_{H_2}/s) was calculated to be $8.7 \times 10^{-6} \text{ mol} \times 6.02 \times 10^{23} \text{ mol}^{-1} / (3600 \text{ s}) \approx 1.45 \times 10^{15} \text{ s}^{-1}$. The amount of incident photons per second ($N_{\text{photons}}/\text{s}$) was calculated to be $(550 \times 10^{-9} \times 9.42 \times 10^{-3}) / (6.626 \times 10^{-34} \times 3 \times 10^8) \approx 2.6 \times 10^{16} \text{ s}^{-1}$. The ratio between N_{H_2}/s and $N_{\text{photons}}/\text{s}$ gives AQE which was determined to be $(2 \times 1.45 \times 10^{15} \text{ s}^{-1} / 2.6 \times 10^{16} \text{ s}^{-1}) \times 100\% \approx 11.20\%$.

Inductively coupled plasma test. As determined by the ICP experiments, the actual Cu loadings in the sample were 3.9 wt% while the experimental loadings were 2 wt%. After the photocatalytic reaction, the Cu loadings were found to be similar (4.3 wt%), which is indicative that the as-prepared plasmonic photocatalysts do not undergo the leaching event during methanol dehydrogenation to hydrogen production. The similar W loadings before and after catalysis, which were 90.8 and 88.0 wt%, respectively, were also received. The ICP analysis further demonstrated that the plasmonic Cu-WC/W nanohybrid sample is highly stable.

Liquid products identification after photocatalysis of methanol over plasmonic 2% Cu-WC/W NPs. The ¹H-NMR spectra before and after reaction for both pure methanol and the liquid-mixture sample are shown in Fig. S25A, B. In ¹H-NMR spectrum, the chemical shifts for methanol (CH₃OH) have two symmetric chemical shifts at around ~3.51 ppm and ~3.16 ppm, which are due to the *J*-coupling between natural-abundance ~1.1% ¹³C and ¹H in CH₃ of methanol that is exhibited in Fig. S25A (24). However, the zoom in on Fig. S25A identifies no other peaks except the reference deuterated methanol (CD₃OH). Over 1000 hours of plasmonic photocatalysis, numbers of new peaks appear as shown in Fig. S25B. The peaks at 8.07 ppm is ascribed to the H of HCOOCH₃ (methyl formate) (25) while peaks at 4.57 ppm correspond to the CH₂ of CH₃OCH₂OCH₃ (methylal) (26). The peak at 3.73 ppm corresponds to the OCH₃ group from both HCOOCH₃ and CH₃OCH₂OCH₃ (25, 26). In addition, the chemical shifts at ~3.73 ppm has spin-spin splitting because of the non-equivalent neighboring atoms.

Measurement of selectivity. The photodecomposition of CH₃OH not only produces hydrogen as a self-separable gas product but also generates methylal and methyl formate as liquid products. After complete photoreaction, we identified the liquid products using GC-FID instrument. From GC-FID experimentation, we obtained corresponding peak areas for methylal and methyl formate. Using standard methylal and methyl formate solution (Figs. S26-27), we formulated a calibration curve to calculate the amount of liquid product. Taking methylal as an example: The obtained peak area of methylal (Fig. 4D in the main text) was determined to be 79.41 pA x min. The amount of methylal was determined to be $79.41 \times 10^5 = -13091.38 + 268580.66 \times X \approx 268580.66 \times X = 79.41 \times 10^5 + 13091.38 \approx X = 29.61$ mole. The produced amount of methyl formate was 6.97 mole. The selectivity of liquid products is calculated based on carbon species formation while the selectivity of methylal was calculated to be $29.61 \text{ mole} / (29.61 \text{ mole} + 6.97 \text{ mole}) \times 100\% = 80.94\%$. In this way, the selectivity of methyl formate was estimated to be 19.06%.

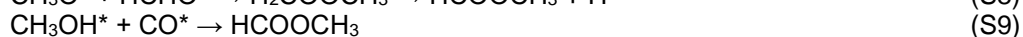
Validation of no CO_x compounds formation. Fig. S30A shows a representative gas chromatogram of a pure methanol solution which displays hydrogen gas at a retention time (RT) of 1.570 min. Fig. S30B, C shows the RT of pure carbon monoxide (CO) and carbon dioxide (CO₂) gases at 3.781 and 12.21 min (27) respectively along with unavoidable air (O₂ at 2.975 min and N₂ at 3.014 min) contamination. Taking the RT of CO and CO₂ as a reference point, we found that the formation of H₂ from methanol dehydrogenation is completely avoiding the evolution of CO and/or CO₂, confirming that the hydrogen production process in this work is a clean, green, environmentally benign, and safe process.

Electron paramagnetic resonance (EPR) experiments with control sample. Neither DMPO (A) nor DMPO with methanol (B) nor DMPO with methanol in the presence of WC/W sample (C) under dark conditions yielded a significant EPR signal (Fig. S31). Even under illumination the WC/W sample failed to produce a reasonable DMPO-CH₃O^{*} free radical adduct signal (D, E, F, G). Therefore, it is expected that the bare WC/W NPs sample is required to hybridize with plasmonic metallic Cu NPs to drive the CH₃OH dehydrogenation reaction to produce H₂ (H, I, J, K).

Methanol dehydrogenation to H₂ and methylal and methyl formate formation under plasmonic excitation. Plasmonic excitation upon visible light illumination can result in energetic charge carriers (hot e⁻-h⁺ pairs) forming on the NPs surface, which has been studied previously in the perspective of chemical reactions transformations (28-30). The extraction of charge carriers and their directional flow towards the catalytic sites in reactive environment could be multistep under plasmonic excitation when considering multimetallic nanohybrid system, for example the Cu-WC/W NPs in this work. We postulate that methanol underwent a multi-hole assisted oxidation processes to yield H₂ under plasmonic excitation at the NPs junction via a direct and indirect charge transfer mechanism (30, 31) at solar light illumination conditions as expressed in reaction 1 and 2. We hypothesize that hot hole mediated CH₃OH oxidation over plasmonic Cu-WC/W NPs can be influenced by multiple factors: (1) modulation of reaction pathways of WC catalyst under perturbation by strain field from W template and electric field from WC LSPR itself, (2) broadband absorption from plasmonic Cu NPs generates energetic charge carriers (hot e⁻-h⁺ pairs) in Cu which flow to the neighbouring WC catalyst because of WC's higher imaginary part of dielectric function than Cu NPs (30, 31), and (3) Cu's LSPR results in direct energetic charge carrier formation at Cu-WC interface via plasmon decay. A cooperative and mutual efforts of these factors play a role in methanol oxidation with proton reduction to H₂ fuel at Cu-WC interfaces.



Once the reaction steps (S1) completed by consuming one hole on WC NP surface, the intermediate, CH₃O^{*} (methoxy species) experiences further oxidation steps (S2) to yield formaldehyde that evolved in existence of second hole. The photoexcitation cycle completed by capture of 2e⁻ to reduce the two available protons for H₂ fuel (S3). In these processes, the formation of second e⁻-h⁺ pair (which provide the second hole for step S2) is critical which needs to be formed within few-μs timescale (the lifetime of CH₃O^{*} is around 4 μs in CH₃OH solution (32)) on NPs immediately after the one hole driven CH₃OH oxidation process. Nevertheless, the availability of HCHO in excess of methanol in the solution to yield methylal (CH₃OCH₂OCH₃) via combination process (33) while the successive decomposition of CH₃O^{*} forms other intermediates species (S4-S6) those participate into multistep reaction pathways to generate methyl formate, HCOOCH₃ (34) is likely to proceed. These formed intermediate species further underwent recombination reactions to yield methyl formate, HCOOCH₃ as shown in reaction S7-S9.



We observed that the formation of HCOOCH₃ is lower as compared to methylal (Fig. 4D in the main text) which indicates that the formation of methyl formate is suppressed in some degree due to the unavailability of methoxy species to induce the reaction S4. This is because the methoxy species were consumed mostly by reaction S2 which is dominating over reaction S4. As a result, the methylal yield is appeared to be faster and progressed rapidly in excess of methanol solution. Reactions S7-S9 are indicating possible ways to make HCOOCH₃ where reaction S7 is considered to be most feasible and selective over reaction S8 and S9. Methyl formate formation via S8 is thought to be indirect pathway because its involvement with dehydrogenation process for intermediate H₂COOCH₃ species (34).

On final note, in addition to the discussed microenvironments role on methanol dehydrogenation to H₂ in the main text, we believed that methanol itself does play vital role too. Indeed, methanol is recognized as a good hole scavenger which could induce multi-hole reaction steps due to hot hole localization (28)

on the surface of WC NPs. In other words, methanol has strong electron-donating capacity on the NPs surface. This corollary indicates that the photoexcited charge carriers under solar light illumination could transfer the excitation to the CH₃OH molecules, with energetic holes and electrons to drive the methanol oxidation and the subsequent proton reduction to H₂ fuel. Parallel observations were made previously in which the presence of hole scavenger could promote the transient photoexcitation at the NPs-molecule interface (35, 36). Moreover, the concentration of hole scavenger can affect the multi-hole driven process, as highlighted that the higher the hole scavenger concentration, the higher the rate of multi-hole oxidation as well as larger the multi-electron reduction process (37). Note that the Cu-WC/W photocatalysts in this work were suspended in the excess pure methanol (purity ~ ≥ 99.9%) during methanol dehydrogenation. Collectively, all these factors play role in triggering the CH₃OH oxidation at the interface as the highly energetic holes interact with the adsorbed CH₃OH molecules, yielding H₂ along with industrially relevant products.

Computational details for excited state. Simulations of excited state reactivity of WC surfaces were investigated using cluster models of the unstrained and strained structures. A representative W₁₂C₁₂ cluster and the reagent were excised from each of the optimized structures. The electronic properties of these models were subsequently computed using the ORCA 5.0.3 software package (38). The ground state was solved using the CAM-B3LPY functional (39), reported to be consistent with coupled-cluster theory for nanoparticles, (40) and the def2-TZVP (41) basis set with an effective core potential for W (42). The lowest 4 singlet–singlet vertical electronic excitations were calculated at the same level of theory by means of time dependent-DFT, using the Tamm–Dancoff approximation. This resulted in the reaction energy diagram (*Supporting Information*, Fig. S35) that qualitatively reproduces the results from plane-wave DFT, in particular, the CH₃O→CH₂O energetic differences (*Supporting Information*, Table S6). Notably, this activation barrier is further reduced upon electronic excitation. The cluster models were also employed to compute the adsorption energies of CH₃OH and CO (*Supporting Information*, Table S7), suggesting the strained structure has a lower adsorption energy for these molecules.

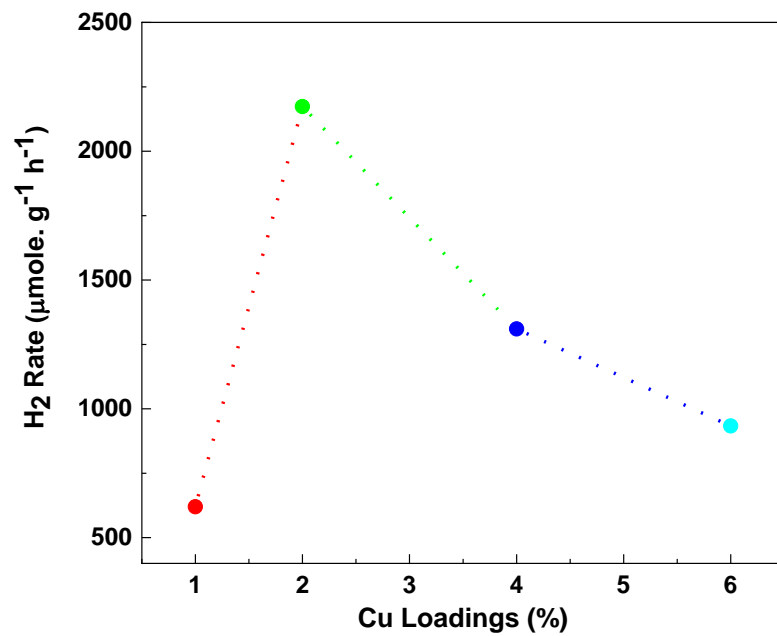


Fig. S1. Effect of Cu precursor loadings on H₂ production from pure CH₃OH solution.

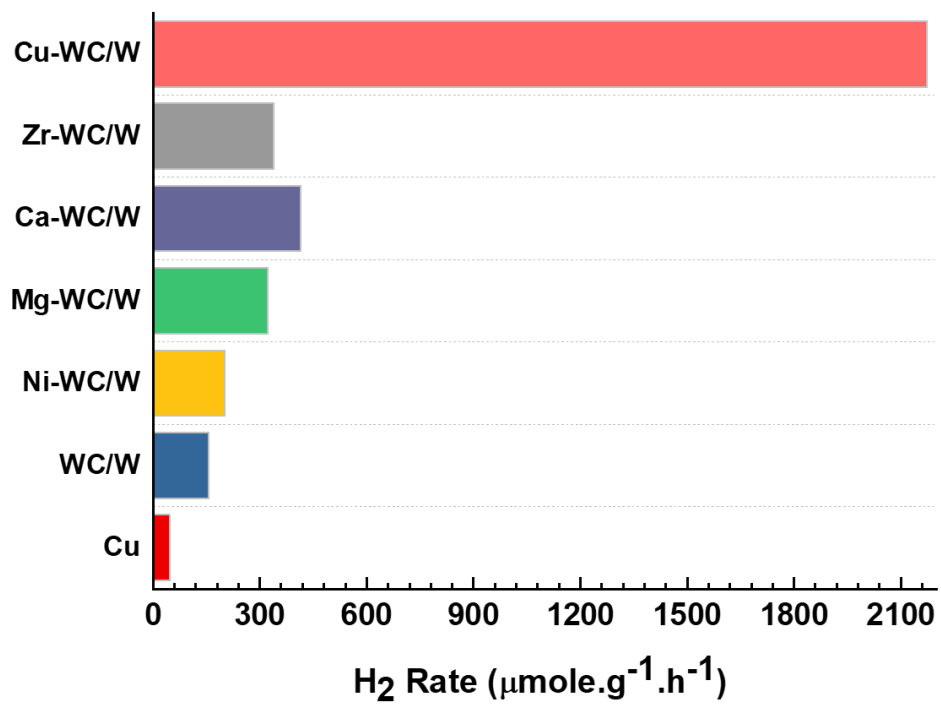


Fig. S2. Effect of noble-free metal loadings to WC/W NPs on H₂ production from pure CH₃OH solution. Based on this results, the hybridization between Cu NPs and WC/W NPs is essential in order to achieve higher photocatalytic performance.

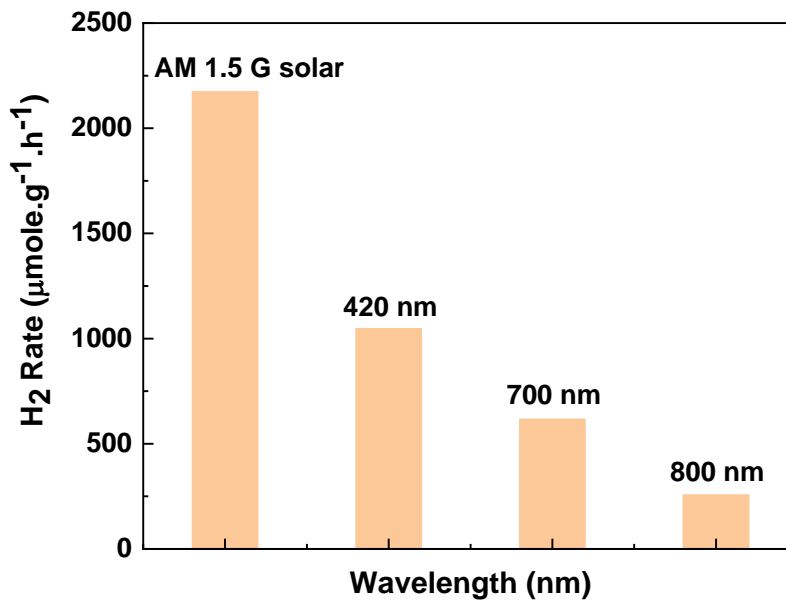


Fig. S3. Effects of various illuminated energy on H₂ formation from pure CH₃OH solution over 2% Cu-WC/W plasmonic nano hybrids. Here, the wavelength of 420, 700, and 800 nm corresponds to the centred wavelengths of the employed band pass filters with 30 nm band width. The output power intensity of 420, 700, and 800 nm band pass filters were measured to be 0.70, 0.18, and 0.07 Watt/cm², respectively, using Thorlabs power meter (Gentec-EO, Canada).

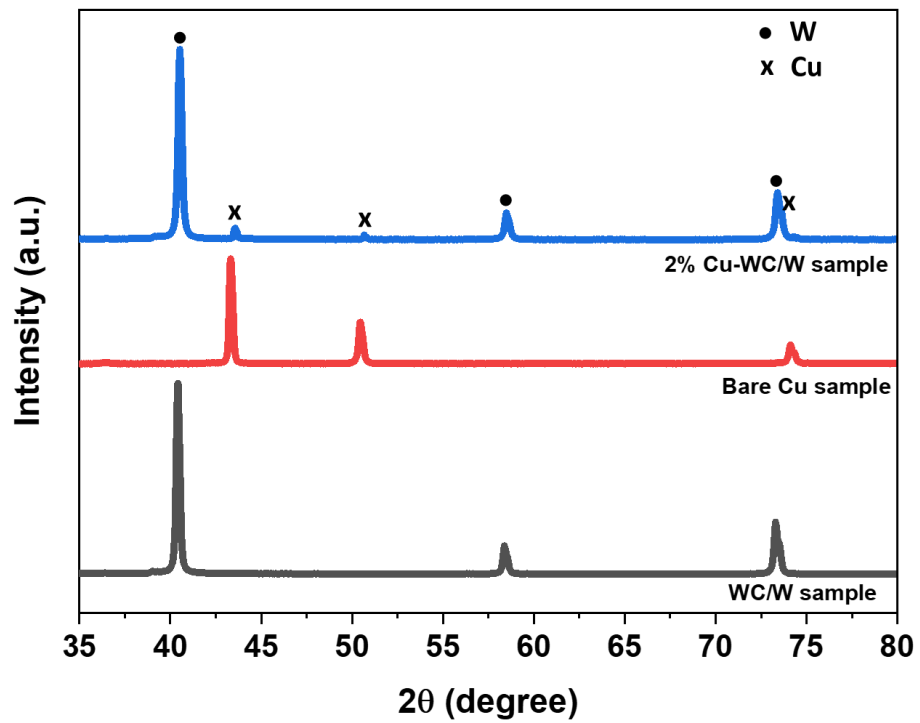


Fig. S4. Powder-XRD characterization of WC/W, Cu and 2% Cu-WC/W catalysts.

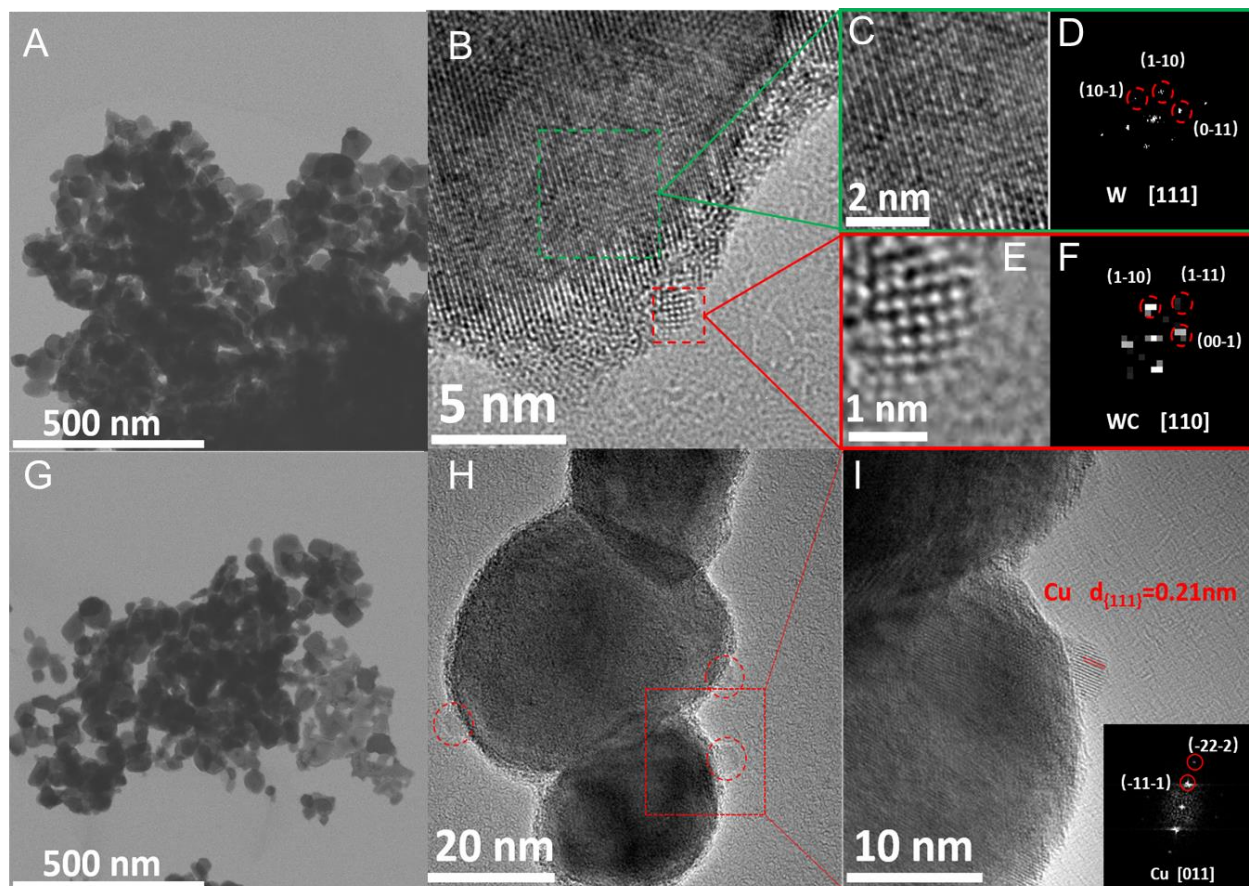


Fig. S5. Aberration-corrected high-resolution TEM analysis of Cu-WC/W photocatalysts. (A) Low magnified TEM image of WC/W sample. (B) TEM image of WC/W sample with high resolution. (C) Representative W NP. (D) The corresponding FFT pattern of the W NP. (E) Representative crystalline WC. (F) The corresponding FFT pattern of WC. (G) Low magnified TEM image of 2% Cu-WC/W sample. (H) Cu NPs are located on the surface of the WC shell. (I) high magnified TEM image of representative Cu particle, and the insert image is the corresponding FFT pattern.

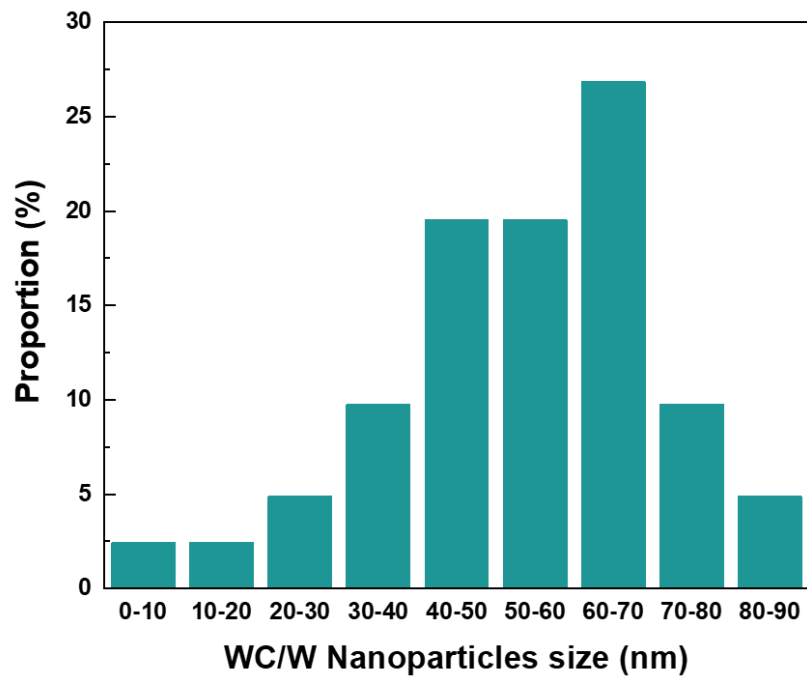


Fig. S6. Nanoparticle distribution of WC/W catalysts.

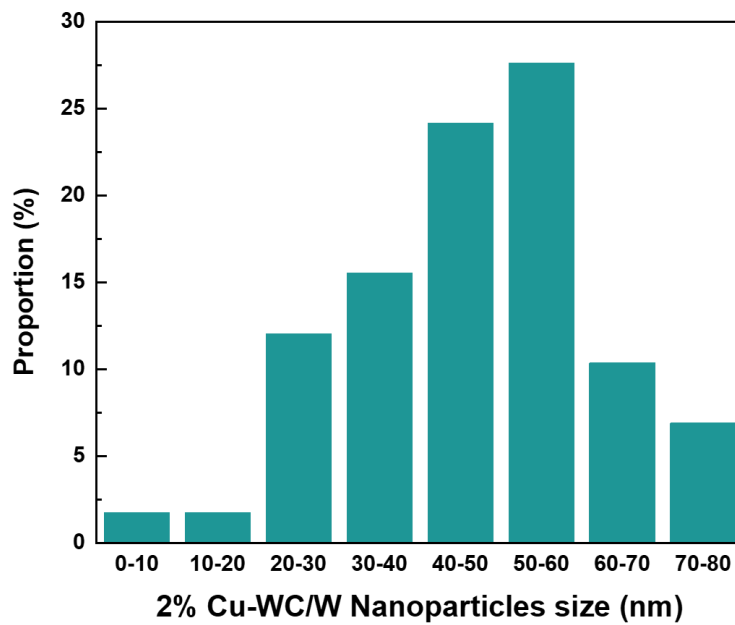


Fig. S7. Nanoparticle distribution of 2% Cu-WC/W catalysts.

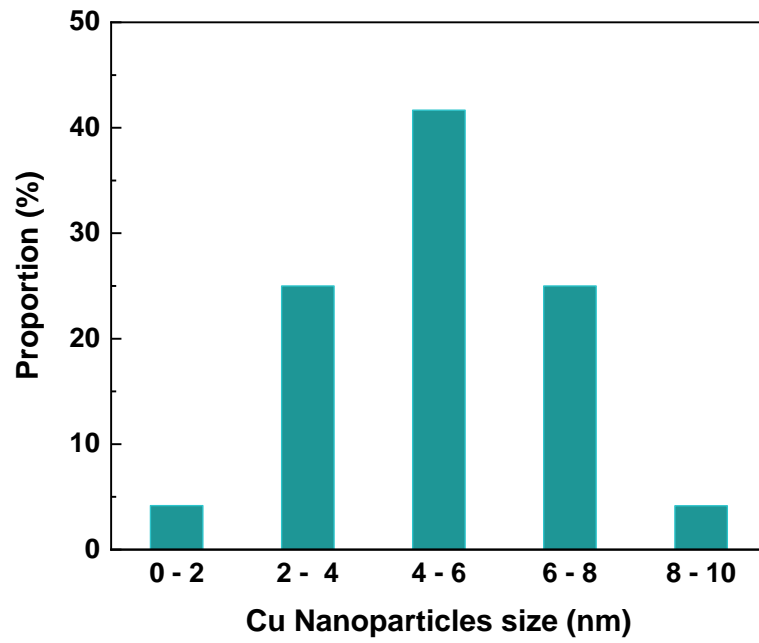


Fig. S8. Cu Nanoparticle size distribution in 2% Cu-WC/W composite.

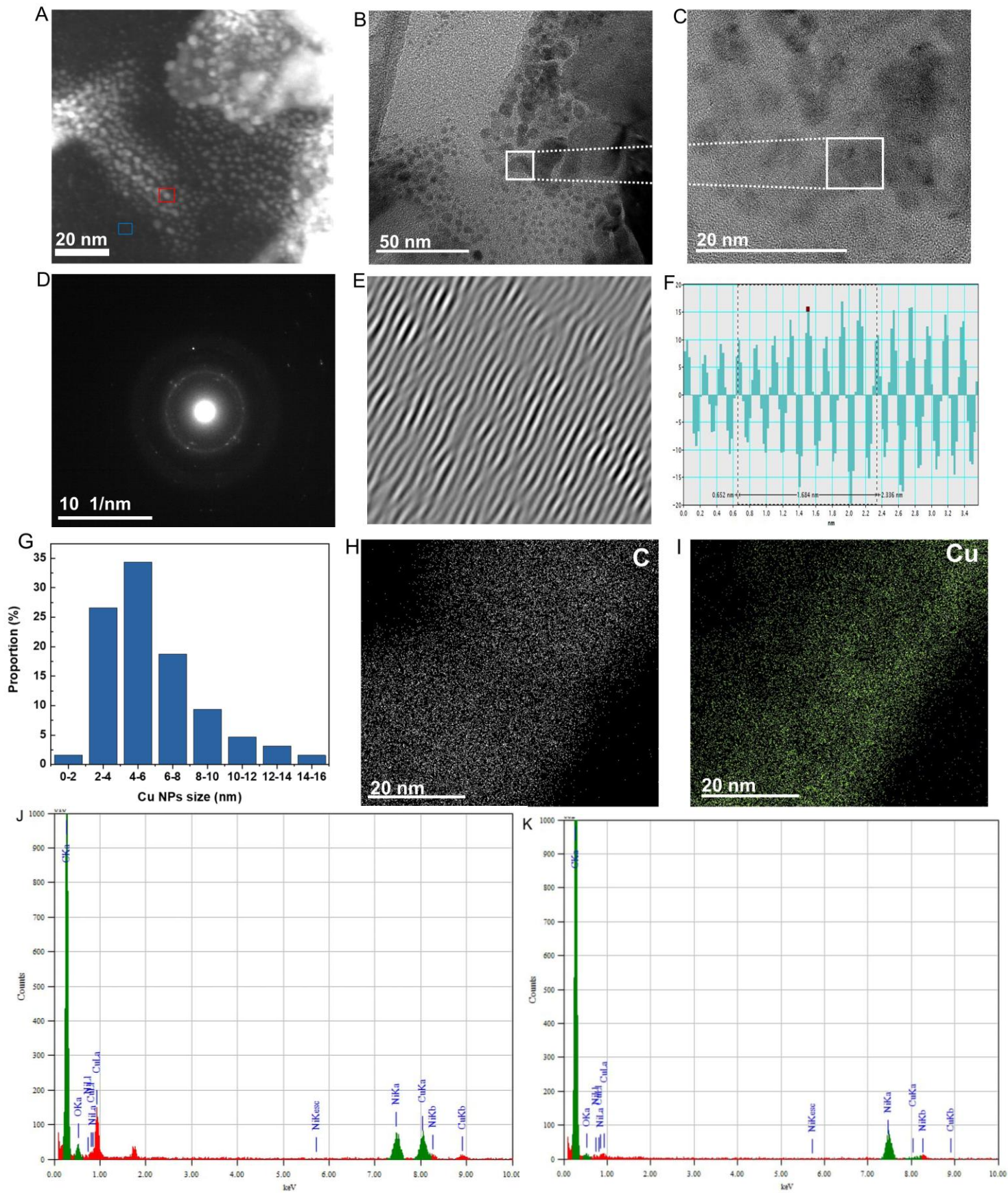


Fig. S9. TEM analysis of bare Cu nanoparticles. (A) STEM-DF image of Cu nanoparticles. (B) HR-TEM at low magnification. (C) HR-TEM at high magnification from small white rectangle area in (B). (D) diffraction pattern of Cu NPs revealed that the lattice distance is about 0.21 nm which corresponds to the (111) plane of Cu NPs. (E) Inverse FFT measured from white rectangle area in (C). (F) Lattice distance measurement via image software from e which estimated to be 0.21 nm that is exactly the same obtained value from (D). (G) Cu nanoparticles size distribution which estimated from (B), which are highly agglomerated and scattered in the surface. (H-I) EDX elemental mapping for C and Cu, respectively, from red and blue rectangle boxes in (A). (J, K) Cu nanoparticles distribution at red and blue rectangle boxes, respectively, in (A). At red rectangle boxes, the co-existence of Cu and C particles is observable whereas there is no Cu particles at blue rectangle box location.

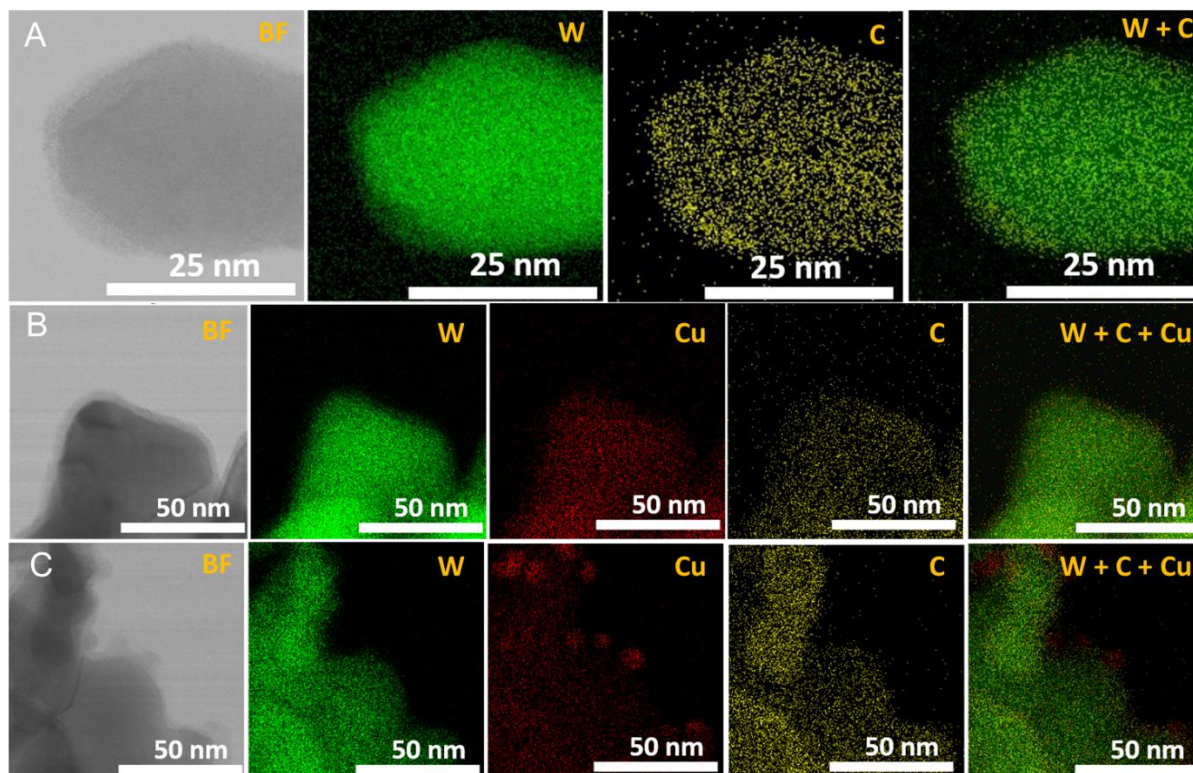


Fig. S10. Bright Field (BF) and EDX elemental mapping. (A) BF image of bare WC/W sample and EDX maps of W, C and W+C. (B) BF image of 1% Cu-WC/W sample and EDX maps of W, C, Cu and W+C+Cu. (C) BF image of 4% Cu-WC/W sample and EDX maps of W, C, Cu and W+C+Cu.

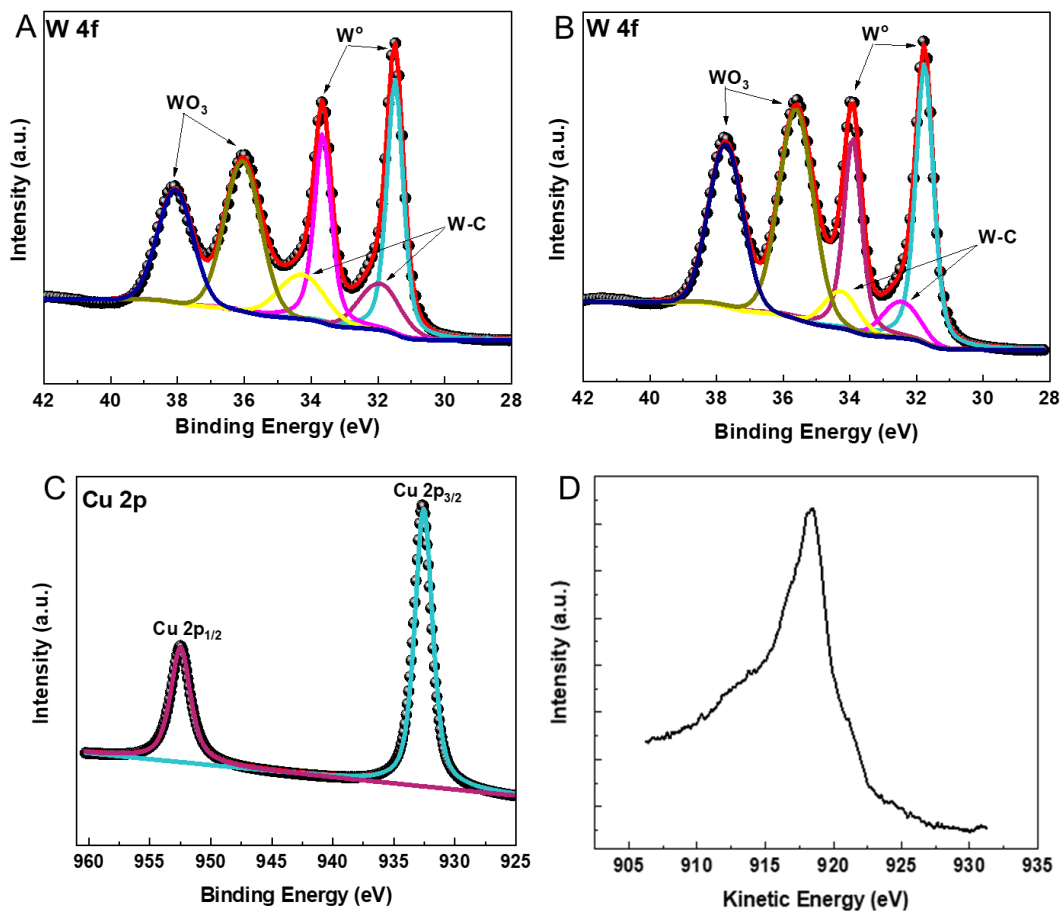


Fig. S11. XPS analysis. (A-B) XPS profile for W4f states before and after introducing Cu. (C) XPS profile for Cu 2p states. (D) Cu LMM Auger spectrum profile.

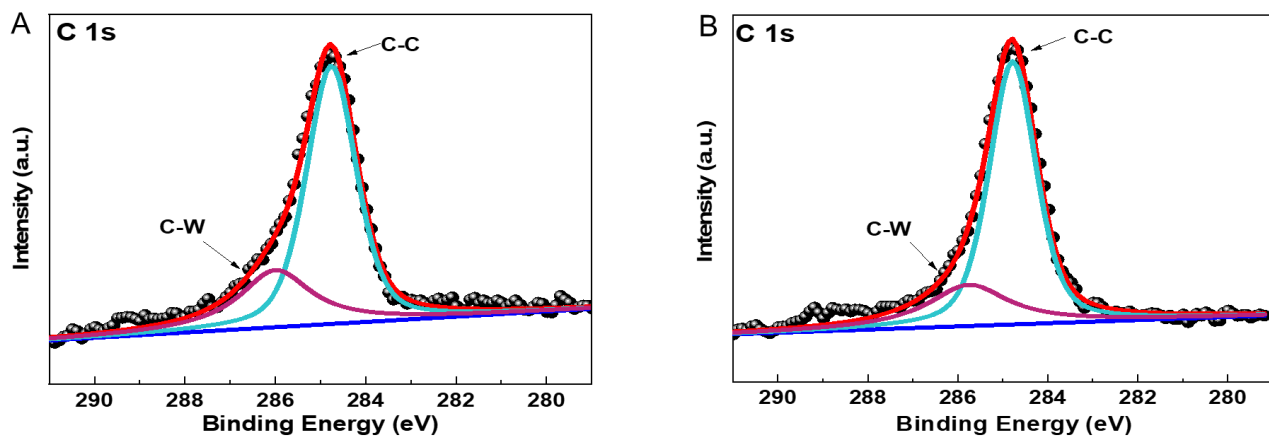


Fig. S12. XPS C1s profile of 2% Cu-WCW NPs sample. (A) Before Cu. (B) After Cu precursor introduction to WCW NPs. The deconvoluted C 1s peak at 286.20 and 284.71eV, corresponds to W-C bonds and sp^3 carbon (C-C) bonds of graphitic carbon. (21, 43-46).

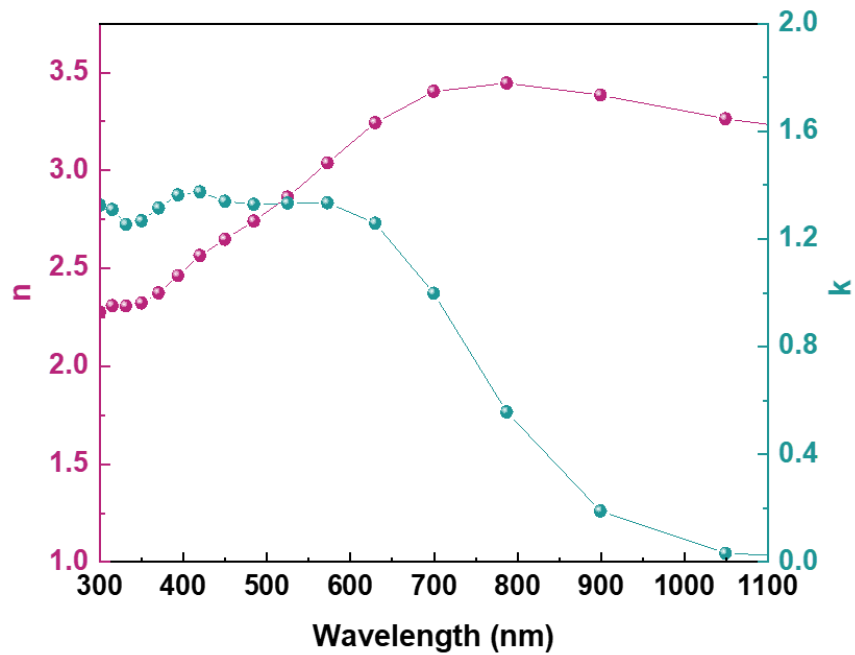


Fig. S13. Refractive index (n) and extinction co-efficient (k) versus wavelength of Cu sample.

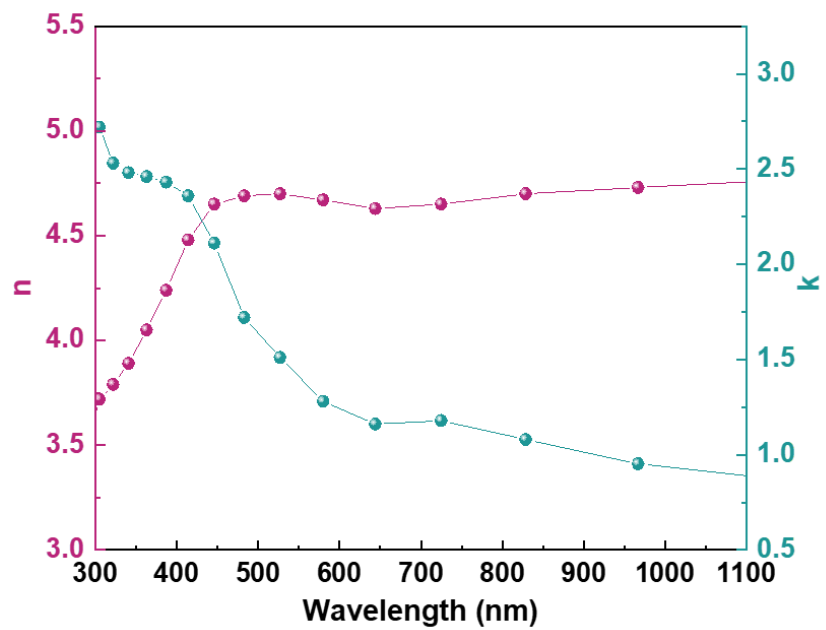


Fig. S14. Refractive index (n) and extinction co-efficient (k) versus wavelength of WC sample.

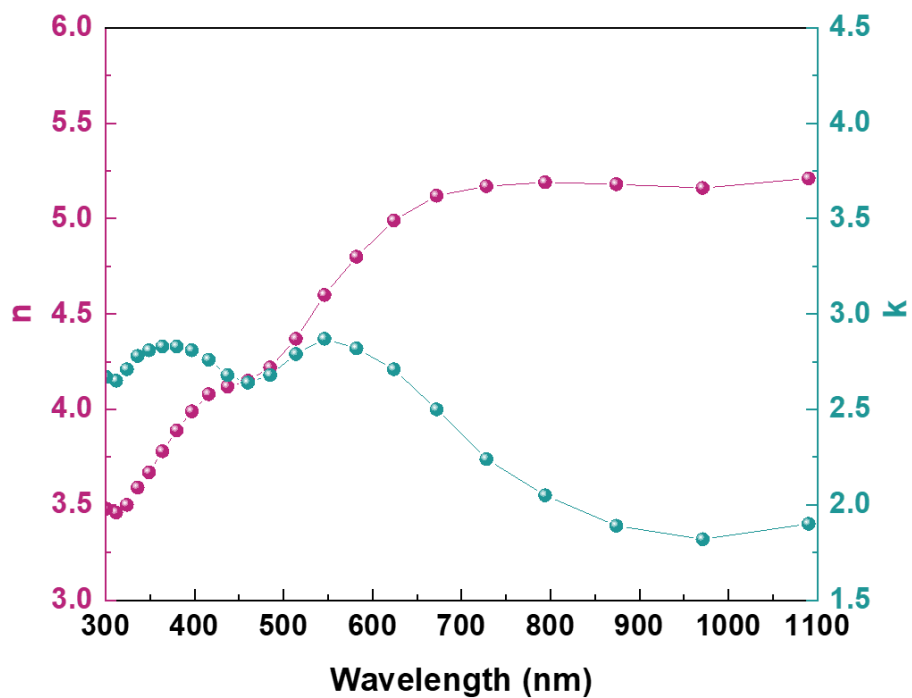


Fig. S15. Refractive index (n) and extinction co-efficient (k) versus wavelength of W sample.

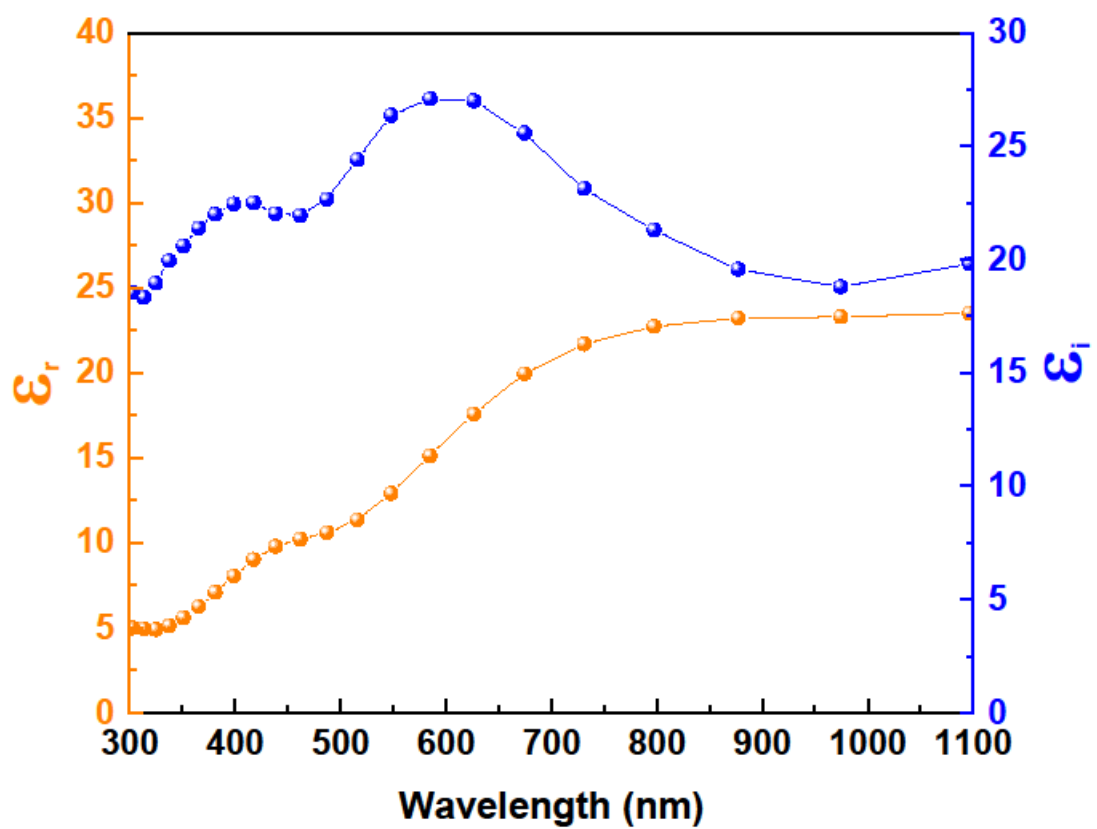


Fig. S16. Dielectric properties versus wavelength of W sample.

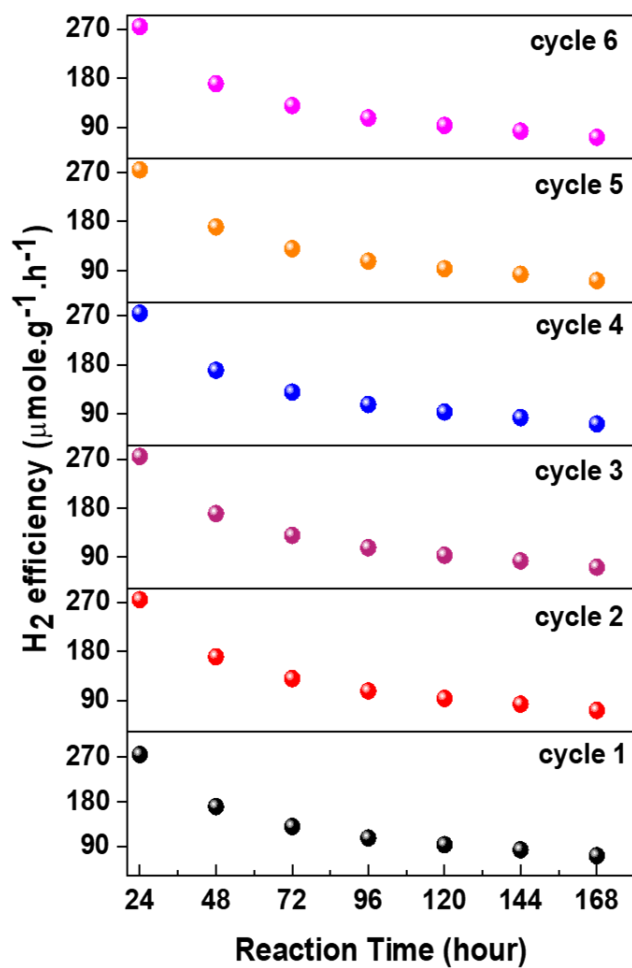


Fig. S17. Representative H₂ efficiency profile over 2% Cu-WC/W NPs for six consecutive tests.

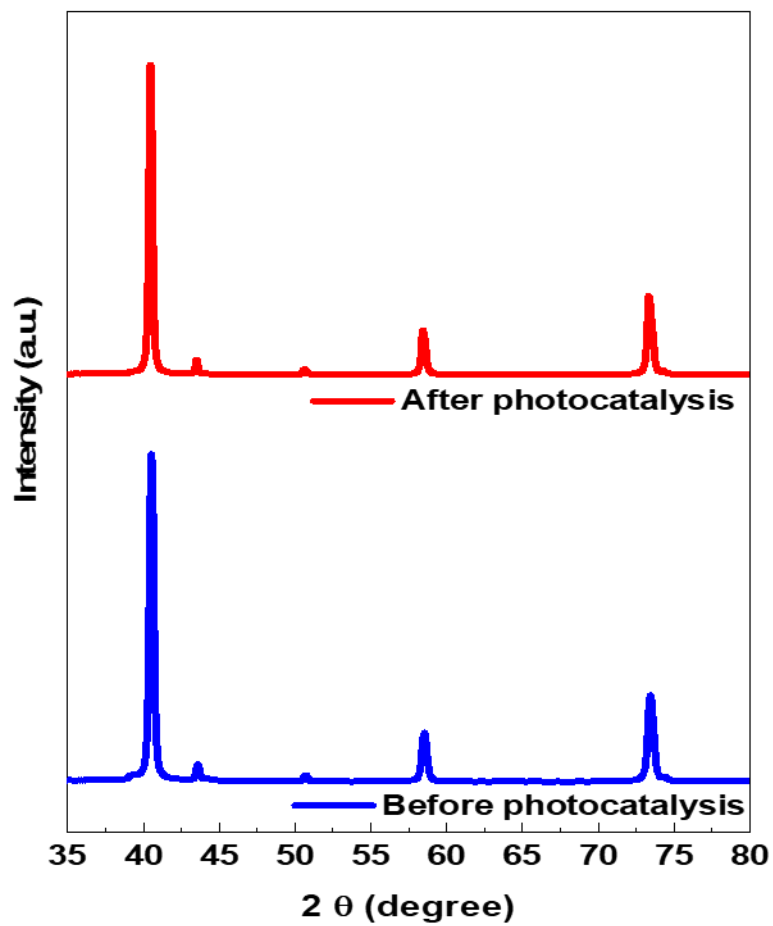


Fig. S18. Representative XRD profile after reaction. As noticed, the shape, size, and the position of corresponding peaks before and after photocatalysis remain unchanged, suggesting highly stable plasmonic catalysts.

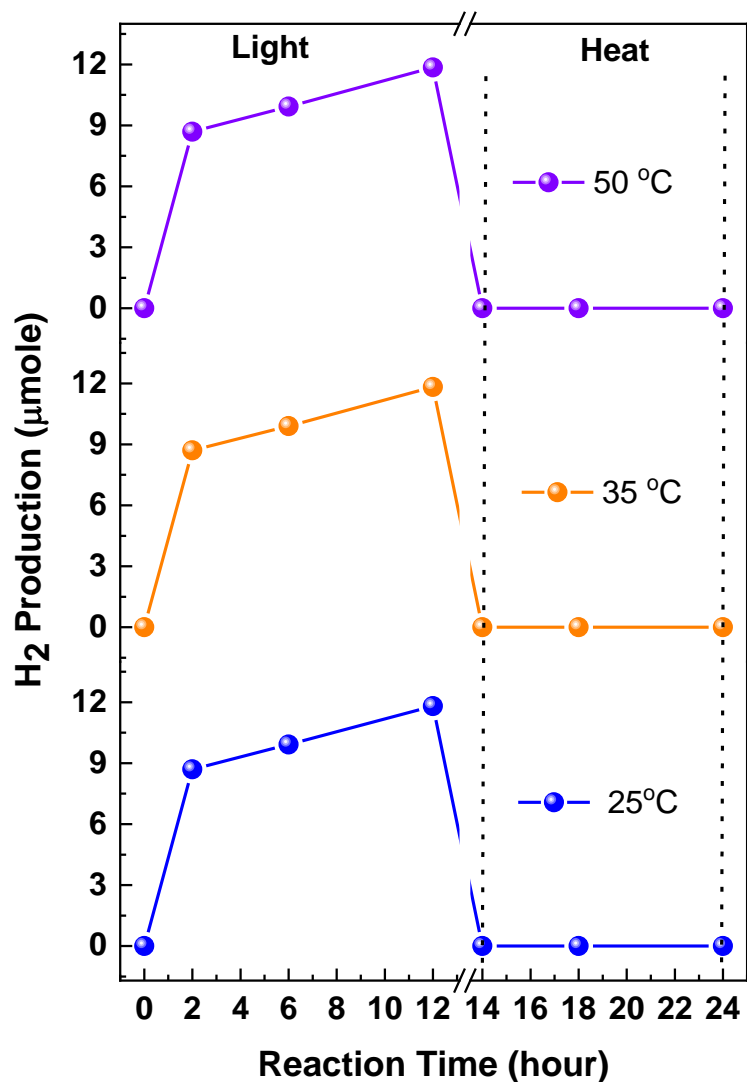


Fig. S19. Photocatalytic heterogeneity test. The data point under two dotted vertical line was obtained during the heating of the filtered methanol solution at 25, 35, and 50 °C. After break point in the x-axis, the data points at 14, 18, and 24 hours are corresponding to the GC analysis for H₂ production after keeping the filtered methanol solution for 2, 6 and 12 hours, respectively, at respective temperature conditions.

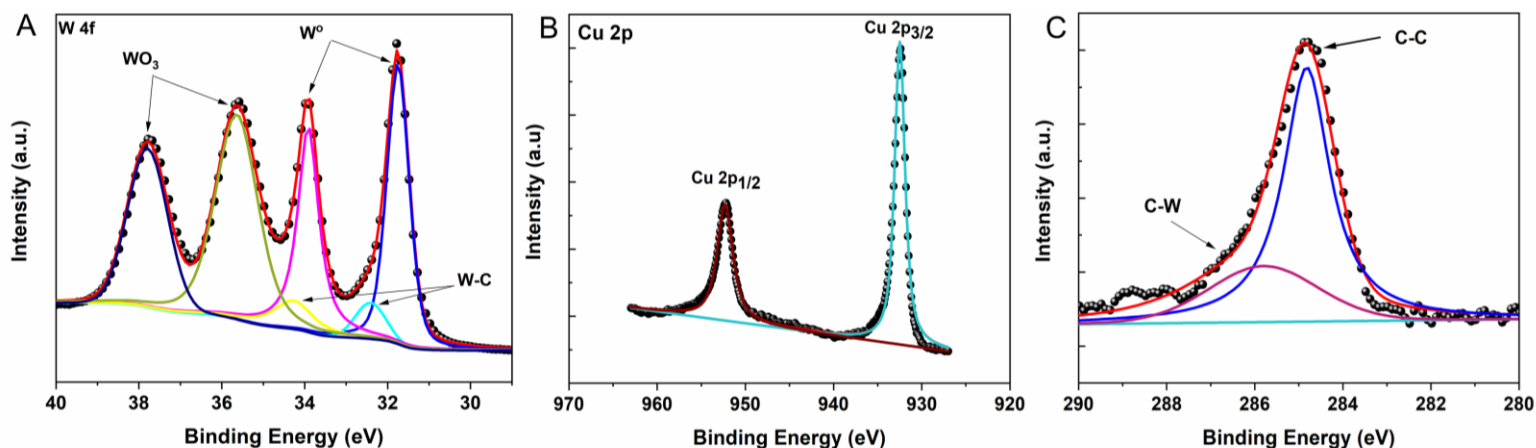


Fig. S20. XPS profile after photocatalytic reaction. (A) W4f, (B) Cu 2p, and (C) C1s XPS spectrum. As observed from after photocatalysis, the plasmonic Cu-WC/W nanohybrids retains its original structure which is verified from the binding energies for W 4f, Cu 2p and C 1s spectrum. The binding energies for major metallic W is around 31.45 and 33.68 eV for W 4f_{7/2} and W 4f_{5/2} respectively (47) while the binding energies for prime Cu 2p peaks at 932.58 eV (48-50). The C1s spectrum shows the representative C-C peak at 284.84 eV (43, 45). All these binding energies values is a direct evidence that the as-prepared plasmonic Cu-WC/W nanostructure keep its original structure after methanol dehydrogenation reaction.

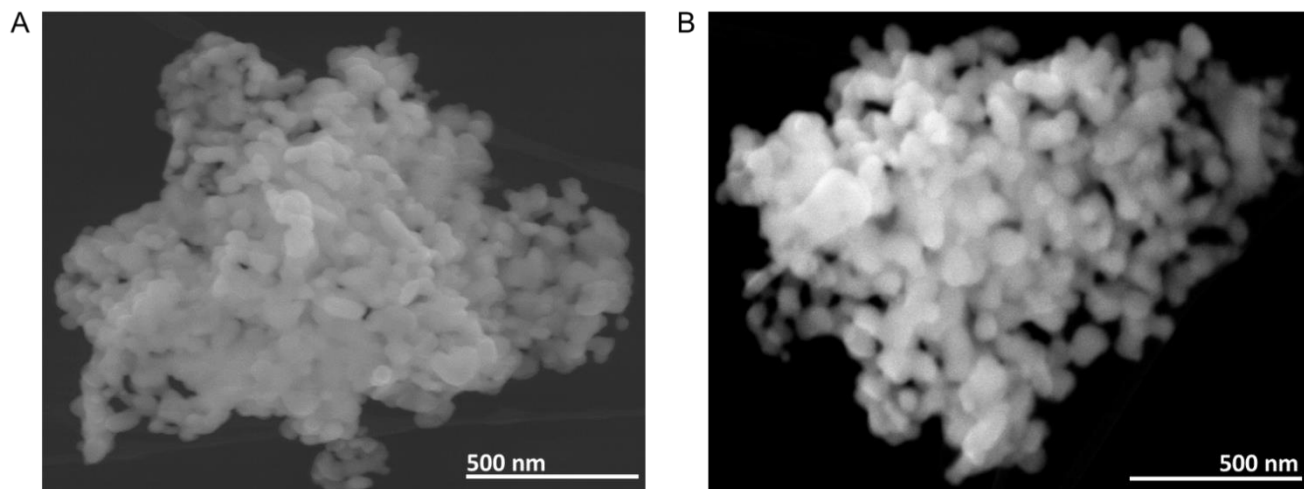


Fig. S21. SEM characterization after photocatalytic methanol dehydrogenation. As is clearly seen from Fig. S21 that before and after methanol photodehydrogenation reaction, the catalysts preserve the similar shape and sizes of the nanoparticles with aggregation morphologies.

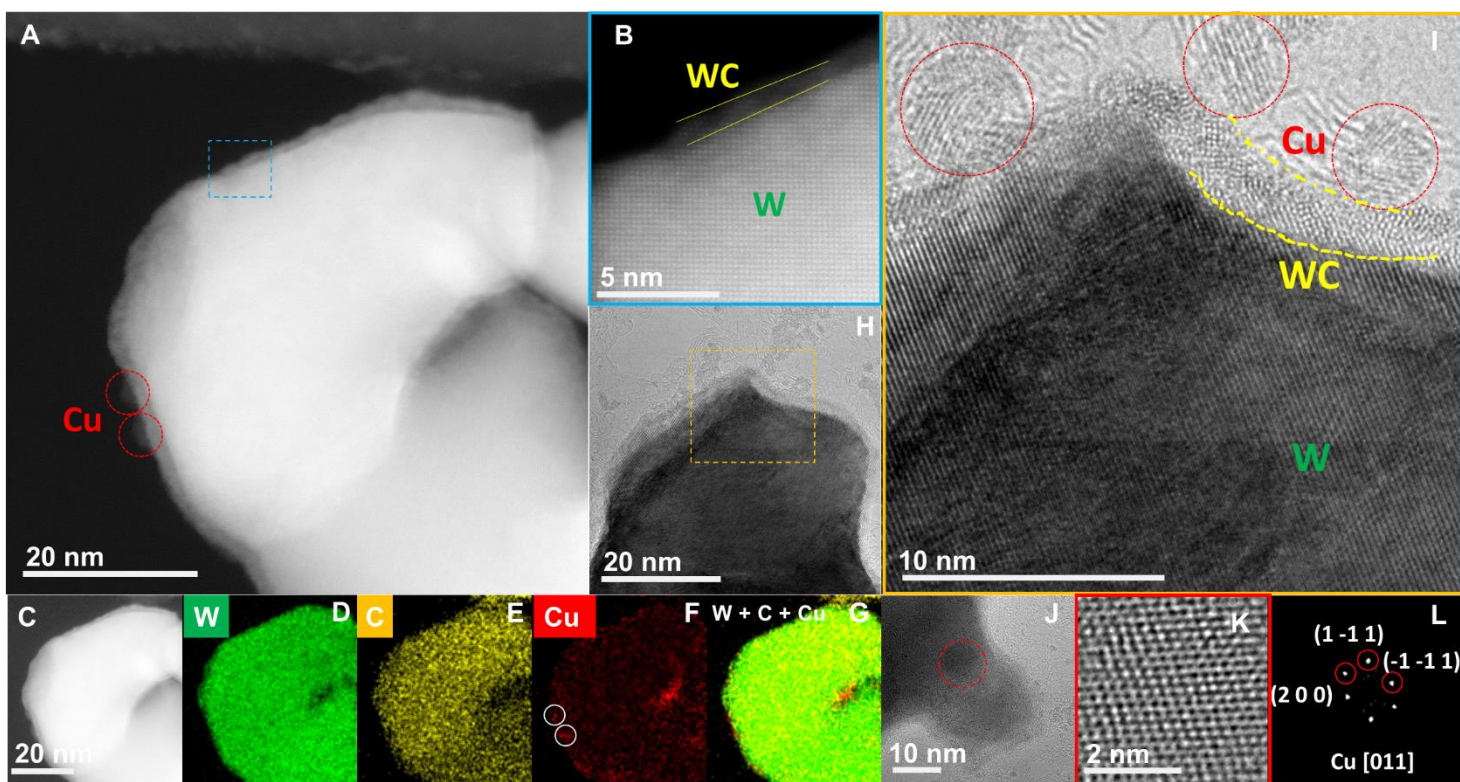


Fig. S22. TEM, STEM and EDS elemental mapping analysis on 2% Cu-WC/W sample after a long term reaction of methanol photodehydrogenation. (A) and (B), representative STEM-HAADF images with atomic resolution, as shown in the images, the core shell structure of sample is well retained and copper nanoparticles keep standing on the surface of WC shell; (C-G) EDX maps of W, C, Cu and W + C + Cu; (H) and (I) representative TEM images with atomic resolution and enlarged image of selected area, the Cu, WC and W components are obviously observed in figure I, which again prove the stability of structures of prepared catalysts, where the Cu NPs are detected on the edges as expected; (J), (K) and (L) a representative top view TEM images of Cu NP located on surface of WC/W, the enlarged image of Cu NP and its corresponding FFT pattern, respectively.

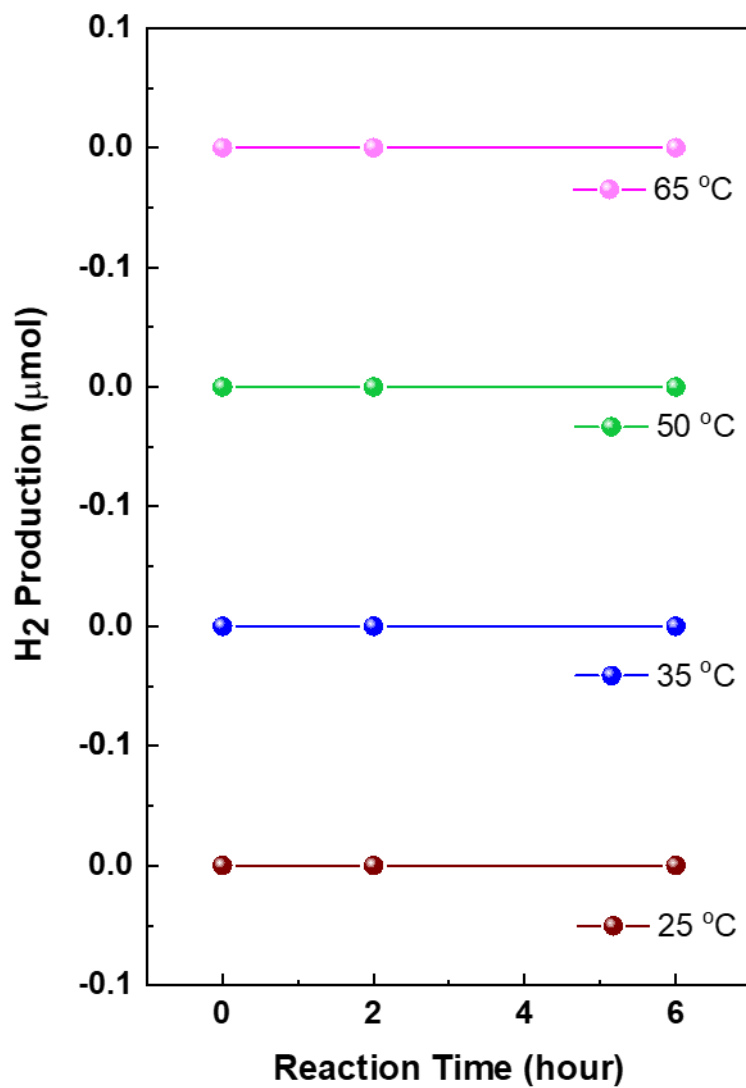


Fig.S23. Analysis of thermal effect at 25, 35, 50 and 65 °C.

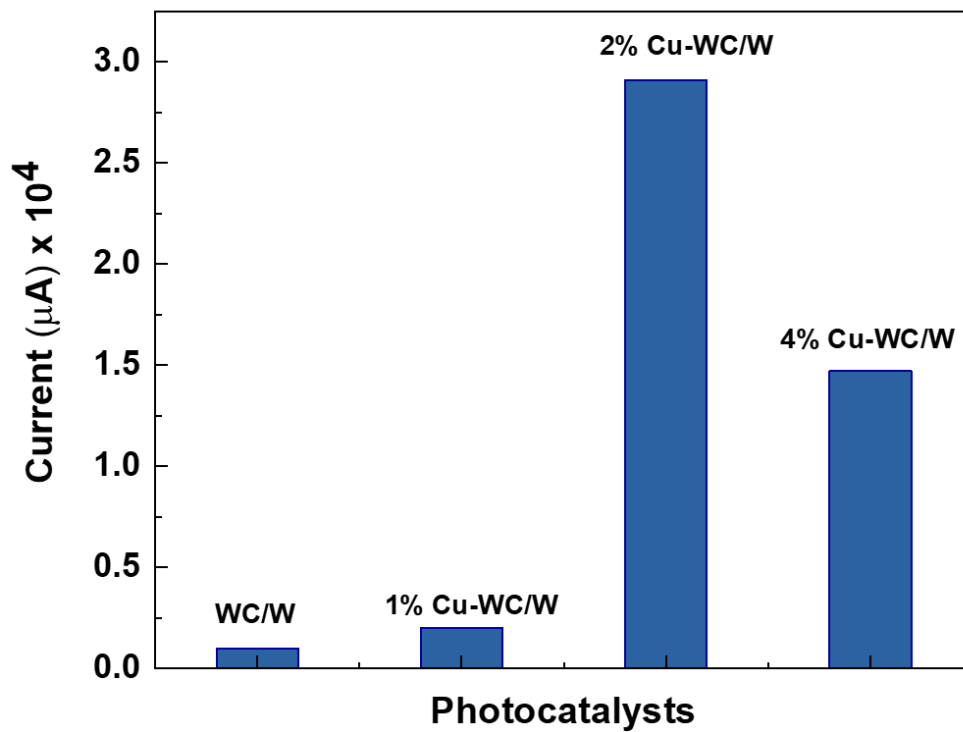


Fig. S24. Photocurrent measurement over various catalysts using solar light at 1.0 V vs RHE in 0.5 M KOH electrolyte containing pure CH₃OH solution.

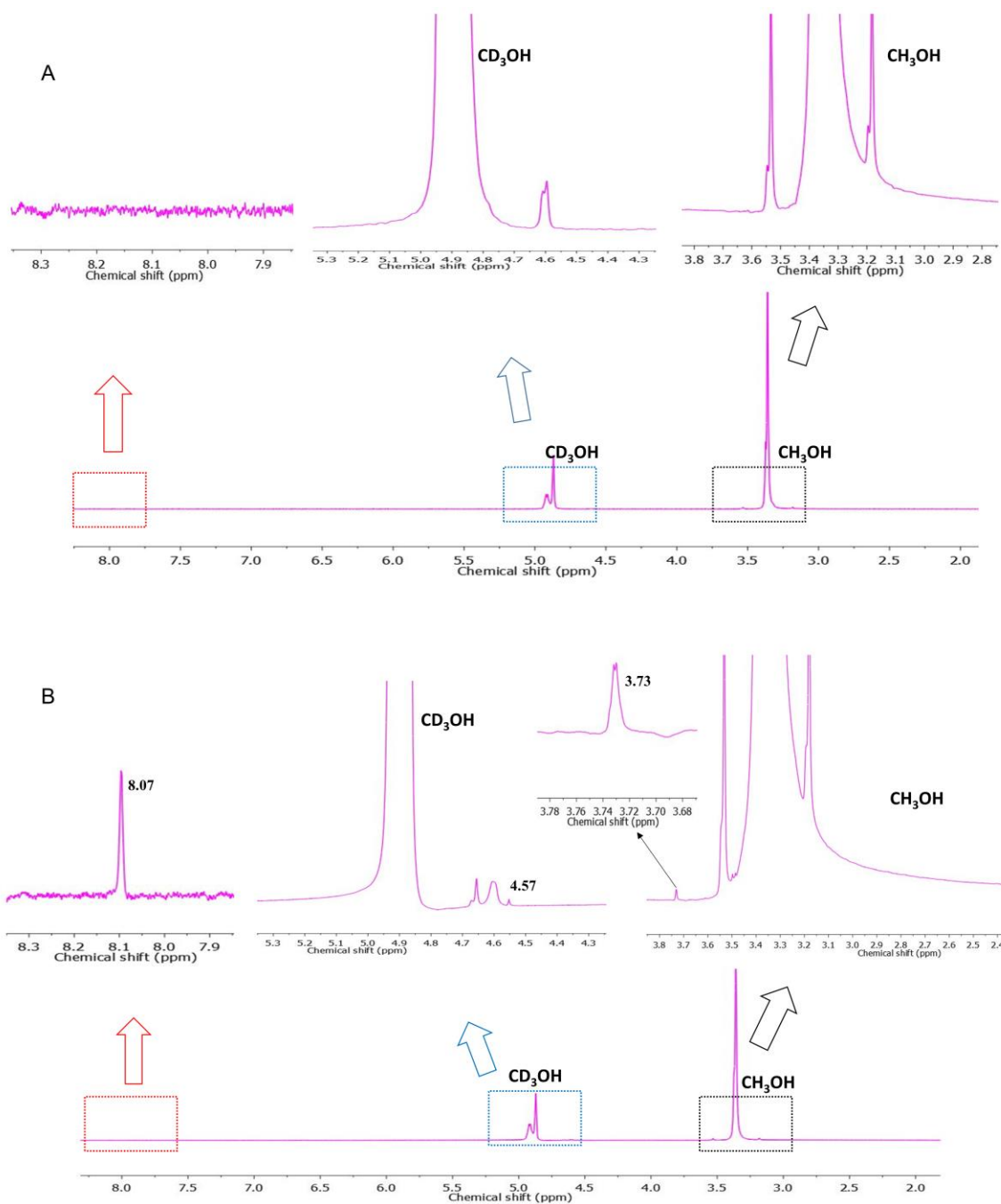


Fig. S25. NMR analysis. (A) ¹H-NMR spectra of pure methanol before reaction. Each colored dotted square box represents the zoom in areas for that particular chemical shifts. (B) ¹H-NMR spectra of methanol after reaction with 2% Cu-WC/W catalysts. The zoom in area after the arrow indicates the new peaks. The ratio of sample to CD₃OD was 4:3 with Bruker 400 MHz instrument.

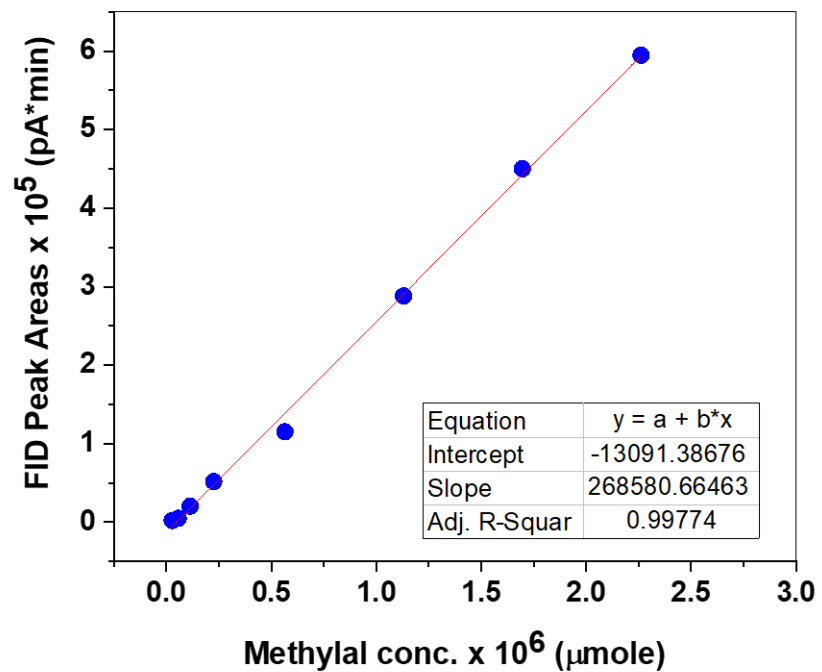


Fig. S26. Calibration curve for methylal products over 2% Cu-WC/W sample.

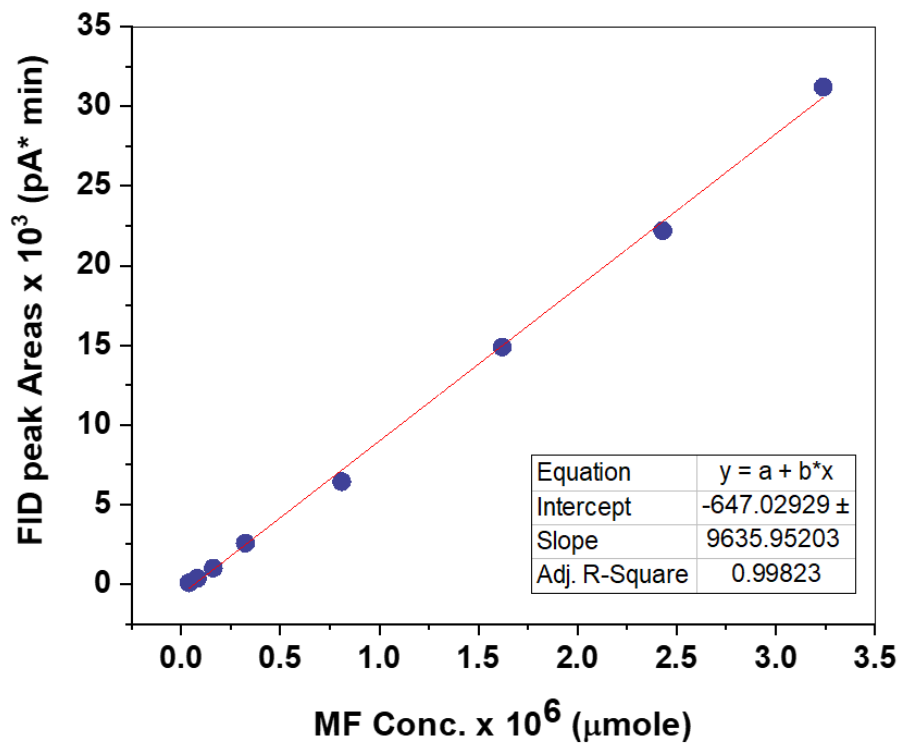


Fig. S27. Calibration curve for methyl formate products over 2% Cu-WC/W sample.

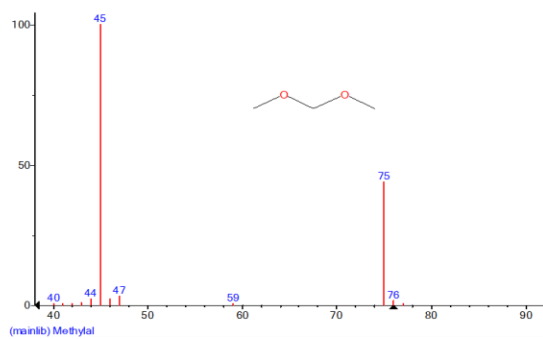
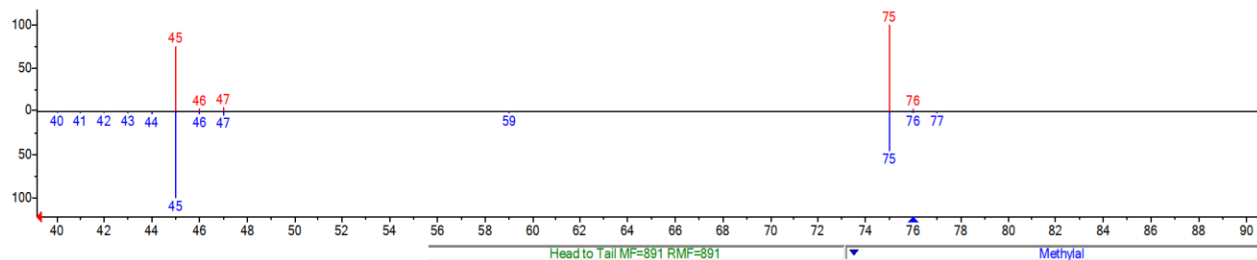


Fig. S28. Observation of methylal products over 2% Cu-WC/W sample. According to GC/MS/MS, methylal $\text{CH}_3\text{OCH}_2\text{OCH}_3$ ($m/e = 76$) was detected as form of $(\text{CH}_3\text{OCHOCH}_3)^+$ ion ($m/e = 75$) after losing one hydrogen atom. Fragmented species, $(\text{CH}_3\text{OCH}_2)^+$ ion at $m/e = 45$ was also observed due to the loss of one methoxy group.

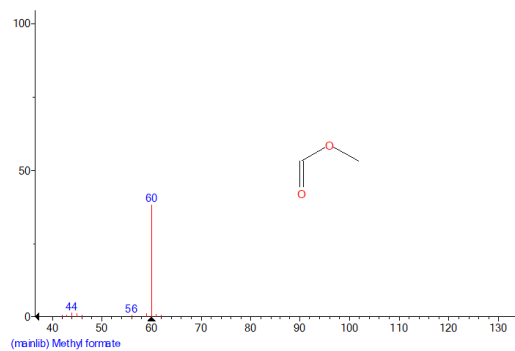
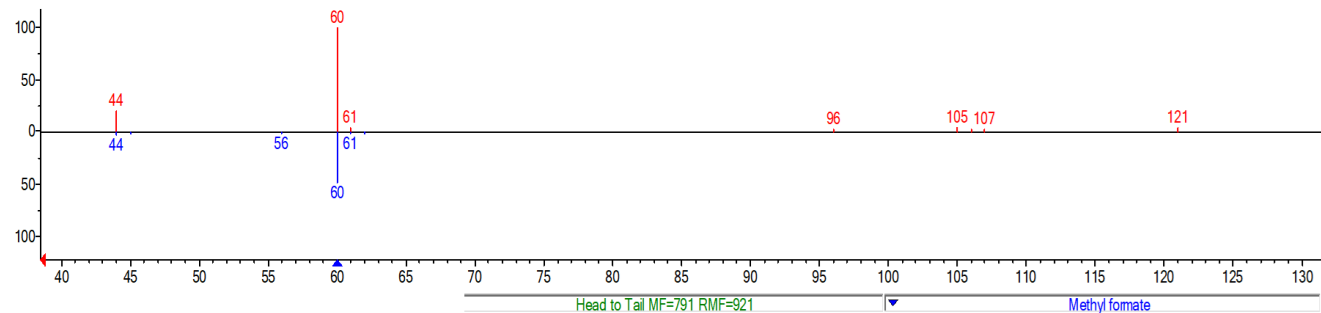


Fig. S29. Observation of methyl formate products over 2% Cu-WC/W sample. Methyl formate was identified as $(\text{HCOOCH}_3)^+$ ion ($m/e = 60$).

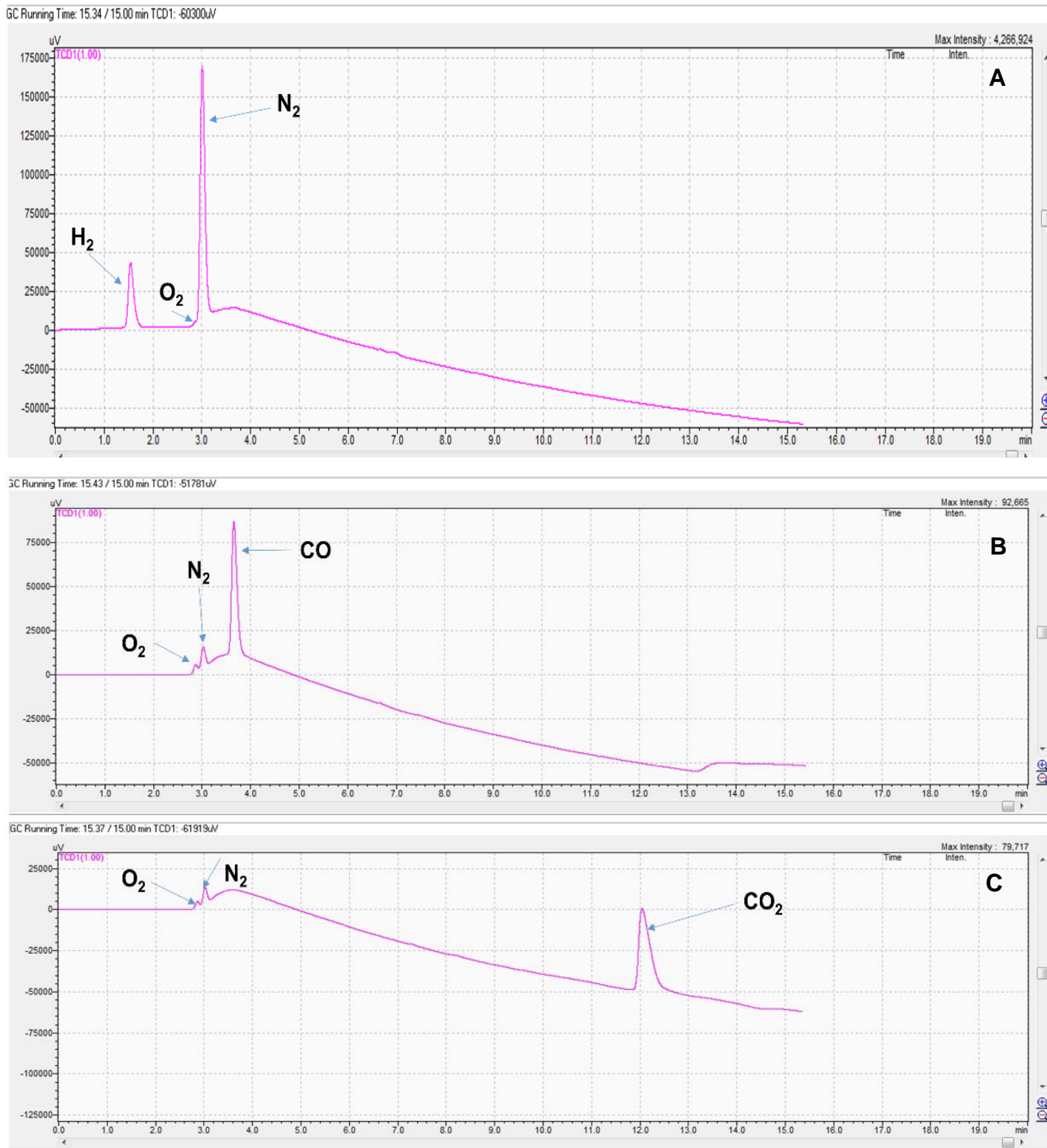


Fig. S30. Verification of no carbon emission from the studied reaction. (A) Analysis of gas chromatography measurement for pure methanol solution. (B) Analysis of pure CO gas. (C) Analysis of pure CO₂.

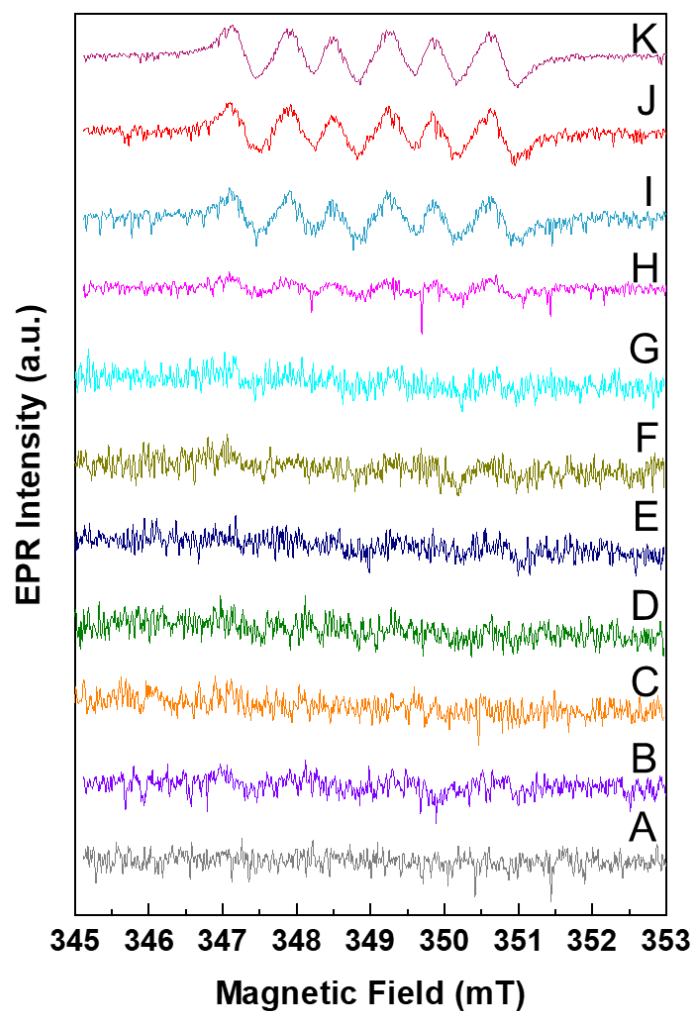


Fig. S31. Electron paramagnetic resonance (EPR) measurement of WC/W NPs sample. The letters corresponds to different EPR tests in the presence of WC/W NPs sample. Here A (DMPO solution in dark), B (DMPO + Methanol in dark), C (DMPO + Methanol + WC/W NPs in dark), D (DMPO + Methanol + WC/W NPs under 1 minute illumination), E (DMPO + Methanol + WC/W NPs under 10 minute illumination), F (DMPO + Methanol + WC/W NPs under 30 minute illumination), G (DMPO + Methanol + WC/W NPs under 60 minute illumination), H (DMPO + Methanol + 2% Cu-WC/W NPs under 1 minute illumination), I (DMPO + Methanol + 2% Cu-WC/W NPs under 10 minute illumination), J (DMPO + Methanol + 2% Cu-WC/W NPs under 30 minute illumination), and K (DMPO + Methanol + 2% Cu-WC/W NPs under 90 minute illumination). In contrast to Fig. 4E-G, all illuminations were performed prior to loading the sample into the EPR spectrometer.

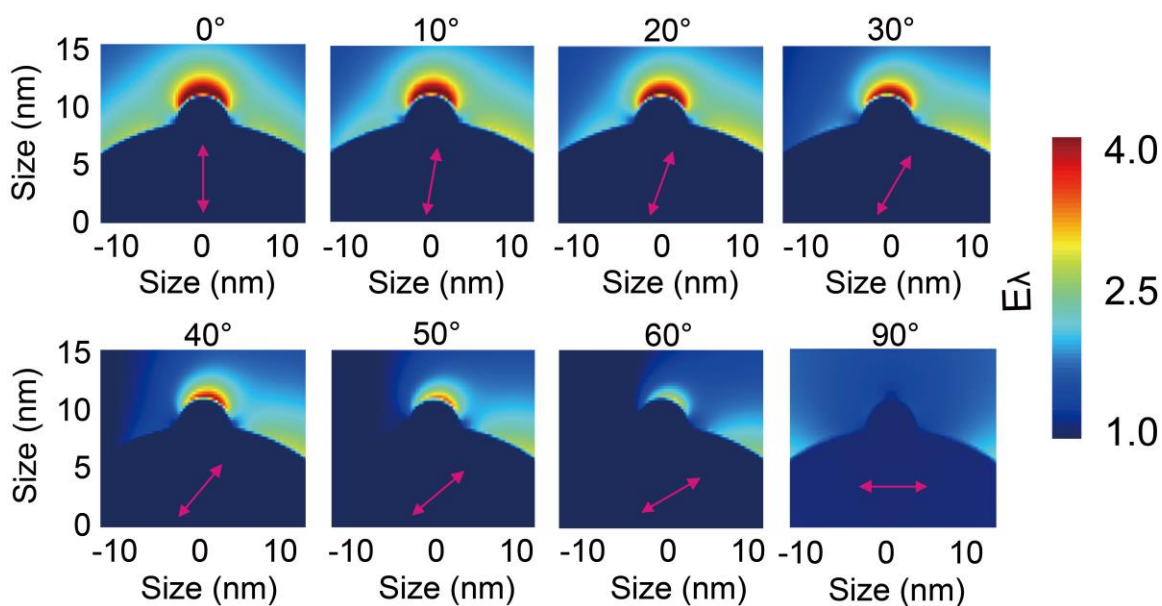


Fig. S32. Finite-difference time-domain (FDTD) simulation for different directions of the incident light relative to the Cu NPs mounted on WC/W. The pink arrow indicates the direction of plane wave.

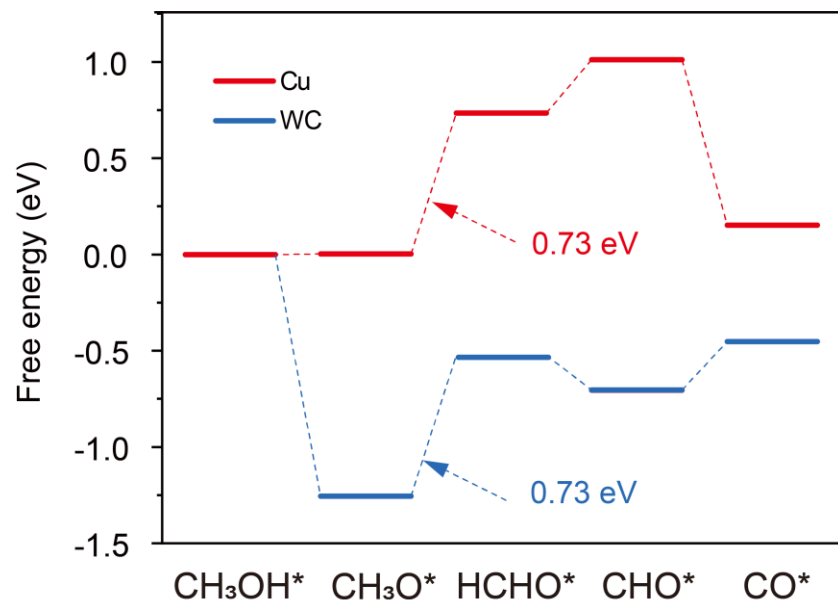


Fig. S33. Free energy diagram for methanol dehydrogenation on Cu, W and WC surface calculated by DFT.

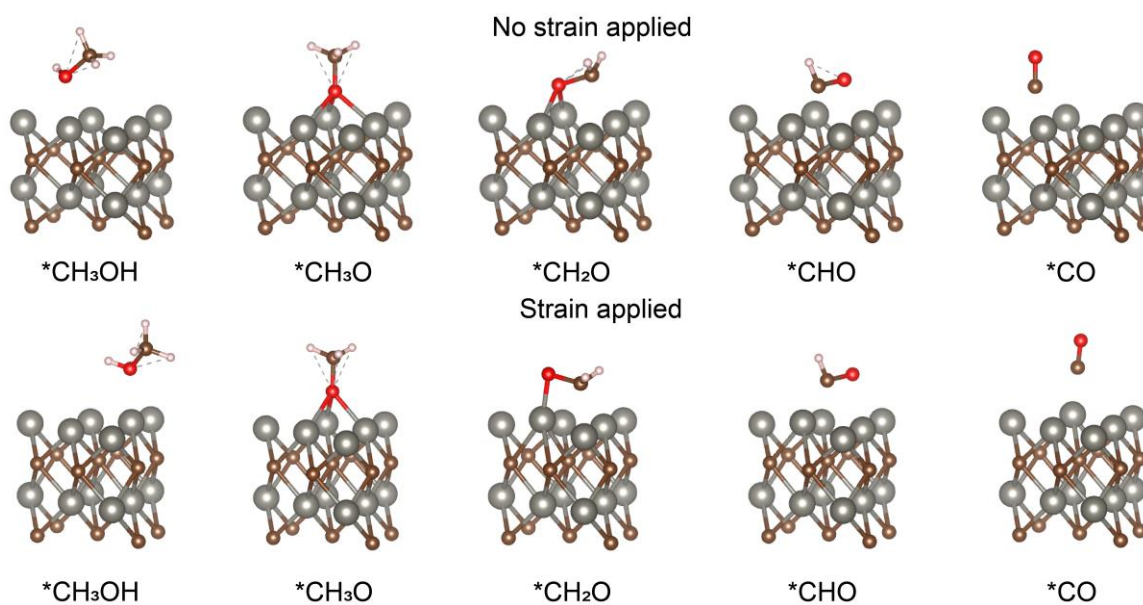


Fig. S34. The representative $W_{12}C_{12}$ cluster and the reagent were excised from each of the optimized structures of the optimized ground-state DFT calculations.

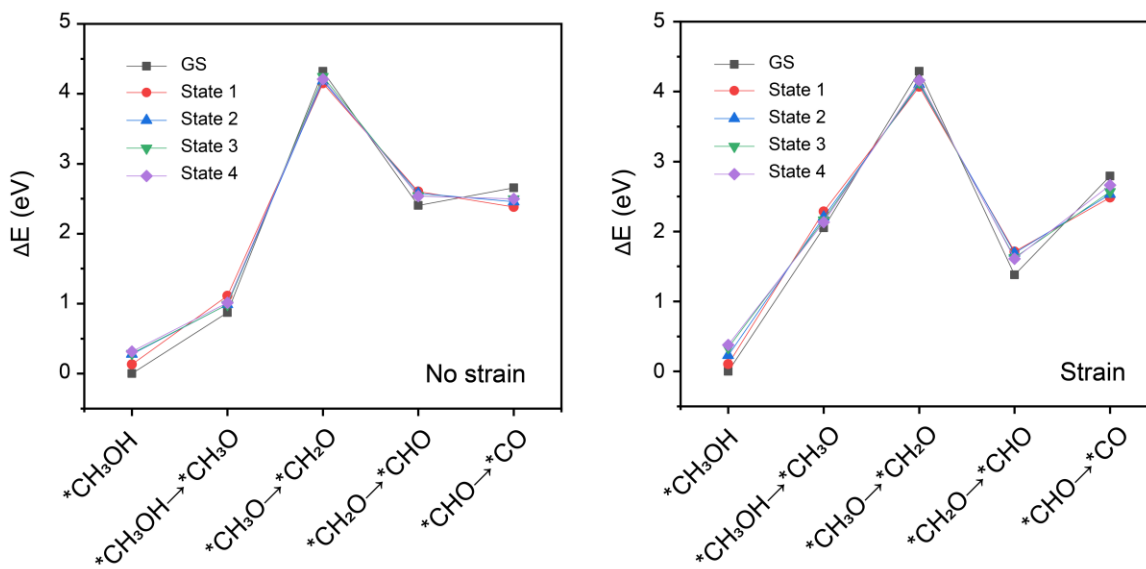


Fig. S35. Relative energy as a function of the reaction coordinate for CH₃OH dehydrogenation reactions on non-strained and strained WC, respectively. A representative W₁₂C₁₂ cluster and the reagent were excised from each of the optimized ground-state DFT calculations. GS: ground state, State 1,2,3,4: excited states.

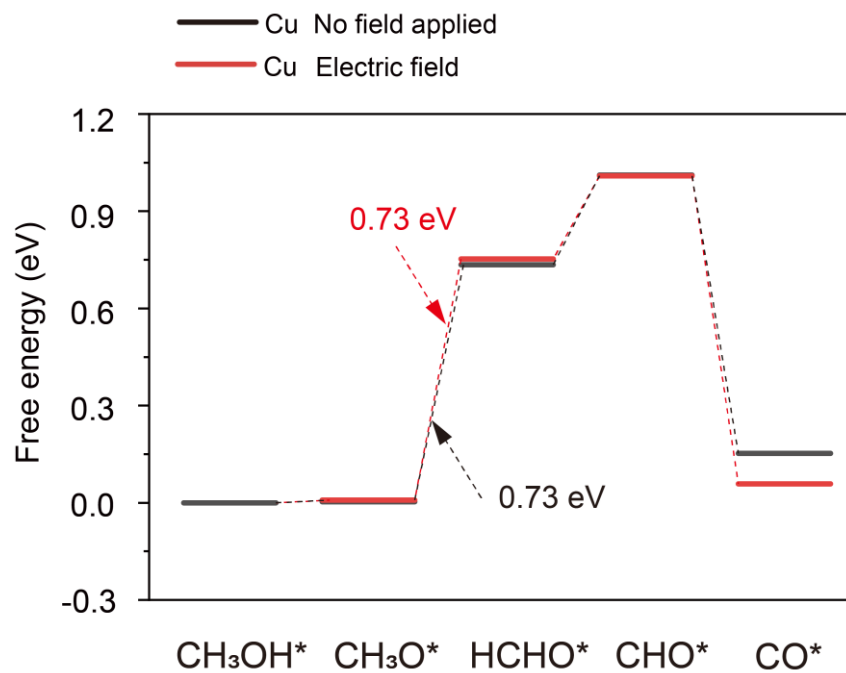


Fig. S36. Free energy diagram for methanol dehydrogenation on Cu surface calculated by DFT, where the perturbations from the electric field were not applied (black line) and applied (red line).

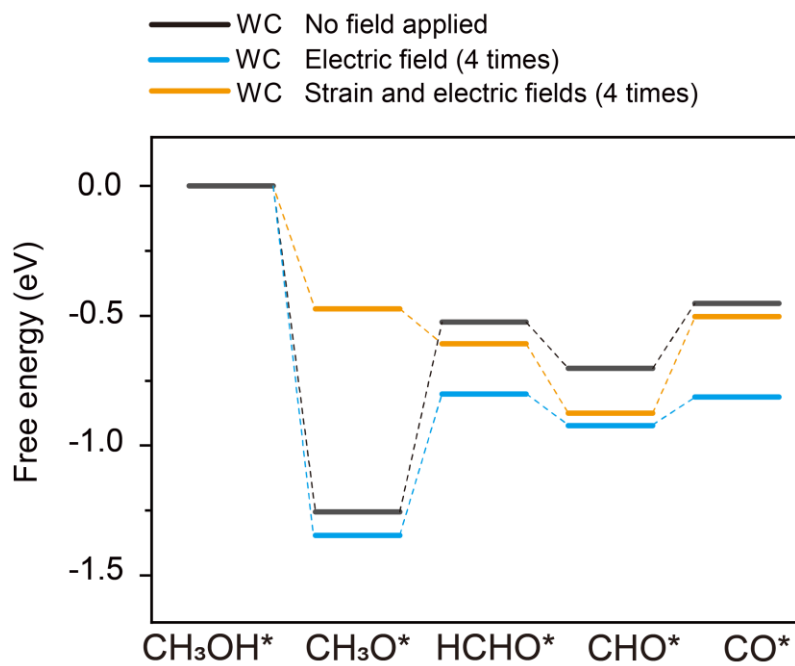


Fig. S37. Free energy diagram for methanol dehydrogenation on WC surface calculated by DFT, where the perturbations from the electric field were applied with different strength.

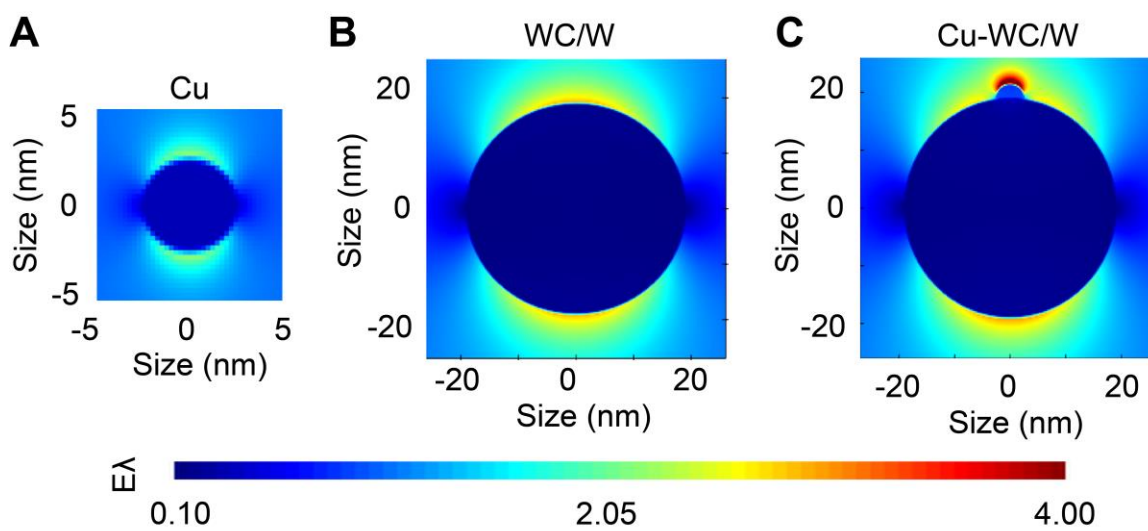


Fig. S38. The FDTD electric field simulation results for 420 nm wavelength of the incident light for (A), Cu, (B), WC/W and (C) Cu-WC/W under the same scale bar.

Table S1. Summarized photocatalytic water splitting and methanol systems for hydrogen production.

No ^a	Photocatalyst	Co-catalyst	H ₂ production rate	Light source	Photoreaction Time (hours/cycle, cycle number, total hours)	Photonic Efficiency (AQE, STH, AQY, EQE, QE, ECE) ^b	Ref
1	TiO ₂ (rutile)	Fe ₂ O ₃	1.16 μmol/h	360-W Hanovia Hg-Arc Lamp	2, 1, 2	n.a	(51)
2	Bi _{0.5} Eu _{0.5} VO ₄	Rh-Cr ₂ O ₃	n.a	450 W Hg lamp (>300 nm)	n.a	n.a	(52)
3	Bi _{0.5} Sm _{0.5} VO ₄	Rh-Cr ₂ O ₃	n.a	450 W Hg lamp (>300 nm)	n.a	n.a	(52)
4	Bi _{0.5} La _{0.5} VO ₄	Rh-Cr ₂ O ₃	n.a	450 W Hg lamp (>300 nm)	n.a	n.a	(52)
5	Bi _{0.5} Eu _{0.25} Y _{0.25} VO ₄	Rh-Cr ₂ O ₃	n.a	450 W Hg lamp (>300 nm)	n.a	n.a	(52)
6	Bi _{0.5} La _{0.25} Y _{0.25} VO ₄	Rh-Cr ₂ O ₃	n.a	450 W Hg lamp (>300 nm)	n.a	n.a	(52)
7	Bi _{0.5} Y _{0.5} VO ₄	Rh-Cr ₂ O ₃	112.7 μmol/h	450 W Hg lamp (>300 nm)	8, 1, 8	n.a	(52)
8	Bi _{0.5} Dy _{0.5} VO ₄	Pt-Cr ₂ O ₃	67.46 μmol/h	300 W Xe lamp (>300 nm)	10, n.a, 28	n.a	(53)
9	Bi _{0.5} Y _{0.5} VO ₄	Pt-Cr ₂ O ₃	86.56 μmol/h	300 W Xe lamp (>300 nm)	n.a, n.a, n.a	n.a	(53)
10	Bi _{0.5} Nd _{0.5} VO ₄	Pt-Cr ₂ O ₃	22.13 μmol/h	300 W Xe lamp (>300 nm)	n.a, n.a, n.a	n.a	(53)
11	Bi _{0.5} Sm _{0.5} VO ₄	Pt-Cr ₂ O ₃	75.30 μmol/h	300 W Xe lamp (>300 nm)	n.a, n.a, n.a	n.a	(53)
12	Bi _{0.5} Gd _{0.5} VO ₄	Pt-Cr ₂ O ₃	26.56 μmol/h	300 W Xe lamp (>300 nm)	n.a, n.a, n.a	n.a	(53)
13	Bi _{0.5} La _{0.5} VO ₄	Pt-Cr ₂ O ₃	61.93 μmol/h	300 W Xe lamp (>300 nm)	n.a, n.a, n.a	n.a	(53)
14	Bi _{1-x} In _x Y _{1-x} Mo _x O ₄	RuO ₂	17 μmol/h	450 W Hg lamp (>420 nm)	10, 4, 40	AQY: 3.2% at 420-800 nm	(54)
15	Sr ₅ Ta ₄ O ₇	NiO	2141 μmol	400 W Hg lamp	6, 1, 6	n.a	(55)
16	In _{0.9} Ni _{0.1} TaO ₄	NiO _x	16.6 μmol/h	300 W Xe lamp (>420 nm)	n.a, 3, 400	QE: 0.66% at 402 nm	(56)
17	In _{0.9} Ni _{0.1} TaO ₄	RuO ₂	8.7 μmol/h	300 W Xe lamp (>420 nm)	n.a	n.a	(56)
18	K ₄ Ta ₂ Nb ₄ O ₁₇	Ni	409 μmol/h	400 W Hg lamp	n.a	n.a	(57)
19	Pr ₂ Ti ₂ O ₇	NiO _x	150 μmol/h/g	450 W Hg lamp (>200 nm)	n.a	n.a	(58)
20	Pr ₂ LaTi ₂ O ₇	NiO _x	220 μmol/h/g	450 W Hg lamp (>200 nm)	n.a	n.a	(58)
21	BaTi ₄ O ₉	RuO ₂	n.a	400 W Xe lamp (>420 nm)	10, 3, 30	n.a	(59)
22	Ga ₂ BiNbO ₇	n.a	72.6 μmol/h	400 W Hg lamp (>420 nm)	n.a, 2, n.a	n.a	(60)
23	In ₂ BiNbO ₇	n.a	54.3 μmol/h	400 W Hg lamp (>420 nm)	n.a, 2, n.a	n.a	(60)
24	CaIn ₂ O ₄	RuO ₂	n.a	400 W Xe lamp	4, 2, 8	n.a	(61)

25	SrIn ₂ O ₄	RuO ₂	n.a	400 W Xe lamp	3, 2, 6	n.a	(61)
26	SrIn ₂ O ₄ :Ba	RuO ₂	n.a	400 W Xe lamp (420-700 nm)	3, 2, 6	n.a	(61)
27	ZnO/Ga-P	RuO ₂	n.a	300 W Xe lamp	n.a, 4, n.a	n.a	(62)
28	(Zn _{1+x} Ge)(N ₂ O _x)	Rh ₂ - vCr _v O ₃	1.58 mmol	450 W Hg lamp (>400 nm)		AQY: 2.0% at 420-440 nm	(63)
29	ZrO ₂ /TaON	IrO ₂ , Cr ₂ O ₃ , RuO _x	n.a	450 W Hg lamp (>300 nm)	2, n.a, n.a	AQY: <0.1% at 420 nm	(64)
30	CaTaO ₂ N	TiOXH, RhCrO _x	n.a	300 W Xe lamp (>420 nm)	10, 3, 30	AQY: 3 × 10 ⁻³ % at 440 ± 30 nm	(65)
31	LaMg _{1/3} Ta _{2/3} O ₂ N	TiOXH, SiOXH, RhCrO _x	n.a	300 W Xe lamp (>300 nm)	24, 2, 48	AQY: 0.03% at 440 ± 30 nm	(66)
32	LaSc _x Ta _{1-x} O _{1+2x} N ₂ -2x	TiOXH, RhCrO _x	n.a	300 W Xe lamp (>300 nm)	5, n.a, n.a	n.a	(67)
33	g-C ₃ N ₄	Pt-Co	1.2 μmol/h	300 W Xe lamp (>420 nm)	n.a, 7, 510	AQY: 0.3% at 405 nm	(68)
34	g-C ₃ N ₄ (nanosheet)	Co ₁ - phosphide	410.3 μmol/h/g	300 W Xe lamp (>420 nm)	3, 4, 12	QE: 3.6%, 2.2%, 0.35% at 420, 500, and 580 nm, respectively STH: 0.16%	(69)
35	Ta ₃ N ₅ (nanorod)	Rh-Cr ₂ O ₃	n.a	300 W Xe lamp (>420 nm)	5, 3, 15	AQY: 2.2%, 0.22% and 0.024% at 320, 420, and 500 nm, respectively STH: 0.014%	(70)
36	Mn(bpy)V ₄ O ₁₁ (bpy)	Pt	92 μmol/h/g	1000 W Xe lamp (420-800 nm)	7, n.a, n.a	n.a	(71)
37	Bi ₂ GaVO ₇	n.a	46.8 μmol/h	400 W Hg lamp (<420 nm)	20, n.a, n.a	n.a	(72)
38	Bi ₂ YVO ₈	n.a	40.7 μmol/h	400 W Hg lamp (at 390 nm)	24, n.a, n.a	Photonic efficiency: 0.628%	(73)
39	BiYWO ₆	Pt-Cr ₂ O ₃	12.3 μmol/h	500 W Xe lamp (>420 nm)	3, 5, 15	n.a	(74)
40	GaFeO ₃ :N	n.a	0.10 μmol/h	300 W Xe lamp (450 ± 5 nm)	6, n.a, n.a	QE: 0.13 ± 0.01% at 450 ± 5 nm	(75)
41	BiOBr	n.a		350 W Hg lamp (>400 nm)	6, n.a, n.a	n.a	(76)
42	BiOI	n.a	1316.9 μmol/h/g	350 W Hg lamp (>400 nm)	6, n.a, n.a	n.a	(76)
43	Bi ₂ Ga ₄ O ₉	RuO _x	19.3 μmol/h/g	300 W Hg lamp (>400 nm)	5, n.a, n.a	n.a	(77)
44	Bi ₂ Ga _{3.6} Fe _{0.4} O ₉	RuO _x	41.5 μmol/h/g	300 W Hg lamp (>400 nm)	5, 7, 35	AQY: 0.09% at 420 nm	(77)
45	Co-P	Black P	15 μmol/h	300 W Xe lamp (≥420 nm)	2, 20, 40	AQE: 42.55% at 430 nm, ECE: over 5.4% at 353 K	(78)

46	CoO nanocrystals	n.a	20 mL	532 nm solid-state laser or an AM1.5G solar simulator	0.5, n.a, n.a	STH: ~5%	(79)
47	SrTiO ₃ :Al	Rh/Cr ₂ O ₃	3.54 mmol/h	300 W Xe lamp	2.5, 5, 12.5	EQE: 95.7%, 95.9% and 91.6% at 350, 360 and 365 nm, respectively STH: 0.65%	(80)
48	SrTiO ₃ :La, Rh/Au/BiVO ₄ :Mo	Cr ₂ O ₃ /Ru	n.a	300 W Xe lamp (> 420 nm)	10, n.a, n.a	AQY: 33% STH: 1.1 %	(81)
49	AgTaO ₃	Rh _{0.5} Cr _{1.5} O ₃	486 mL/m ² /h	AM1.5G solar simulator	10, n.a, n.a	AQY: 40% STH: 0.13 %	(82)
50	CdS/boron carbonitride nanotubes	n.a	526.02 μmol/h/g	300 W Xe lamp (> 420 nm)	5, 10, 50	AQY: 4.01%	(83)
51	NiCo ₂ S ₄ /ZnIn ₂ S ₄ /Co ₃ O ₄ yolk-shell	NiCo ₂ S ₄	20 μmol/h	Xenon lamp (> 400 nm)	3, 3, 9	n.a	(84)
52	Red P/C ₃ N ₄ vdW heterostructure	n.a	239.8, 128.9, 65.3, 26.7, and 367 μmol/h/g at 420, 500, 560, 620 nm and full arc irradiation, respectively.	300 W Xe lamp (> 420, 500, 560, 620 nm and full arc irradiation)	5, n.a, 28	n.a	(85)
53	P/ CDots-C ₃ N ₄	Pt-CoP	619.5 μmol/h/g	300 W Xe lamp (> 420 nm) and AM 1.5G solar simulator	3, 8, 24	AQE: 6.8% at 400 nm and 2.4% at 500 nm	(86)
54	BiVO ₄ / ZnIn ₂ S ₄	Ti ₃ C ₂ MXene QDs	102.67 μmol/h/g	300 W xenon lamp (> 400 nm)	4, 5, 20	AQY: 2.4, 2.9, 1.4, and 0.2 % at 410, 460, 510, and 560 nm, respectively.	(87)
55	Fe ₂ O ₃ /C ₃ N ₄	Pt	3.7 μmol/h	AM 1.5G solar simulator	4, 4, 16	AQE: 7.1% at 365 nm	(88)
56	Polymeric C ₃ N ₄ /LaOCl	n.a	22.3 μmol/h	AM 1.5G solar simulator	5, 5, 25	AQE: 0.35 % at 400 nm	(89)
57	CQDs/CdS	Ni ₄ P ₂	145 μmol/h/g	LED light source (= 420 nm)	3, n.a, n.a	AQE: 0.57 % at 420 nm	(90)
58	g-C ₃ N ₄	Co ₃ (PO ₄) ₂	375.6 μmol/h/g	Xenon lamp (> 400 nm)	3, 4, 12	AQE: 1.32 % at 420 nm	(91)
59	Cd _{0.5} Zn _{0.5} S	n.a	137.2 μmol/h/g	300 W Xe lamp (> 420 nm)	5, 3, 15	AQY: 0.34 % at 400 nm	(92)
60	Red P/Cd _{0.9} Zn _{0.1} S	CoP	1167 μmol/h/g	300 W Xe lamp (> 420 nm)	4, 3, 12	AQE: 6.4 % at 420 nm	(93)

61	GaNZnON/ InP core-shell nanoparticles	Rh	1128 $\mu\text{mol/h/g}$	300 W Xe lamp (400, 450, 500, 550, and 600 nm, respectively)	n.a	AQE: 10.6% % at 430 nm and 13.8% at 350 nm	(94)
62	TiO ₂ nanofilm	Pt	n.a	4 W mercury lamp	n.a	n.a	(95)
63	2D SnS/g-C ₃ N ₄ heterojunction	n.a	1.27 mmol/h/g	300 W Xe lamp AM 1.5G solar simulator	120, 3, 360	AQE: 5.78% at 550 nm STH: 2.46 %	(27)
64	MgO NPs	n.a	320 $\mu\text{mol/h/g}$	1000-W mercury lamp	12 ^c , 3, 48	n.a	(24)
65	N-doped TiO ₂	Pt, Pd, Ir, Rh, Ru	n.a	15 W germicide lamp	n.a	n.a	(96)
66	N-doped TiO ₂	Au	n.a	15 W germicide lamp	n.a	n.a	(97)
67	Li _{2-x} H _x Ti ₃ O ₇ Na _{2-x} H _x Ti ₃ O ₇ K _{2-x} H _x Ti ₃ O ₇ and Cs _{2-x} H _x Ti ₃ O ₇ , respectively	Pt	262 243 327 and 219 μmol , respectively	30 W UV lamp	3, n.a, n.a	n.a	(98)
68	2D MoS ₂ nanosheets	n.a	617 $\mu\text{mol/h/g}$	300 W Xe lamp AM 1.5G solar simulator	66, 3, 198	n.a	(99)
69	Ti-beta	n.a	0.01204 mmol/g	4 W mercury lamp	3, n.a, n.a	n.a	(100)
70	g-C ₃ N ₄ aerogel	AgNPs	152.2 $\mu\text{mol/h/g}$	300 W xenon-lamp (350–780 nm)	7, 3, 21	n.a	(101)
71	Cu-WC/W nanoparticles	n.a	2.176 mmol/h/g	300 W Xe lamp AM 1.5G solar simulator	168, 6, 1008	AQE = 11.20% STH = 2.40%	This work

^aEntry number 1-61 represents the photocatalysts utility for water splitting system while entry number beyond 61 corresponds to application in pure methanol dehydrogenation.

^bPhotonic efficiency: quantum efficiency (QE), apparent quantum yield (AQY), solar to hydrogen efficiency (STH), apparent quantum efficiency (AQE), energy conversion efficiency (ECE), and external quantum efficiency (EQE)

^cFirst and second cycle run for 12 hours respectively, and third cycle run for 24 hours

n.a: data not given or not available

Table S2. Tested the convergence of layer number for surface energy DFT calculation for Cu.

Layer Number	Surface Energy (eV/Å ²) 1,0,0	Layer Number	Surface Energy (eV/Å ²) 1,1,0	Layer Number	Surface Energy (eV/Å ²) 1,1,1	Layer Number	Surface Energy (eV/Å ²) 2,1,1	Layer Number	Surface Energy (eV/Å ²) 2,2,1	Layer Number	Surface Energy (eV/Å ²) 2,1,0
4	0.09	6	0.10	3	0.08	8	0.09	12	0.09	8	0.10
6	0.09	8	0.09	4	0.08	12	0.09	16	0.09	12	0.10
8	0.08	10	0.10	5	0.08	16	0.09	20	0.09	16	0.10

Table S3. Tested the convergence of layer number for surface energy DFT calculation for W.

Layer Number	Surface Energy (eV/Å ²) 1,0,0	Layer Number	Surface Energy (eV/Å ²) 1,1,0	Layer Number	Surface Energy (eV/Å ²) 1,1,1	Layer Number	Surface Energy (eV/Å ²) 2,1,1	Layer Number	Surface Energy (eV/Å ²) 2,2,1	Layer Number	Surface Energy (eV/Å ²) 2,1,0
4	0.25	3	0.21	8	0.23	6	0.22	12	0.23	12	0.23
6	0.25	4	0.20	10	0.22	8	0.21	16	0.23	16	0.23
8	0.24	5	0.20	12	0.21	10	0.21	20	0.22	20	0.23

Table S4. Calculated the surface energy and Work function for Cu surface with low Miller index (<3).

Cu Miller Indices (hkl)	1,0,0	1,1,0	1,1,1	2,1,1	2,2,1	2,1,0
Surface Energy (eV/Å ²)	0.08	0.1	0.08	0.09	0.09	0.1
Surface Energy (J/m ²)	1.35	1.52	1.25	1.47	1.44	1.63
Work Function (eV)	4.45	4.36	4.63	4.41	4.46	4.28

Table S5. Calculated the surface energy and Work function for W surface with low Miller index (<3).

W Miller Indices (hkl)	1,0,0	1,1,0	1,1,1	2,1,1	2,2,1	2,1,0
Surface Energy (eV/Å ²)	0.24	0.2	0.21	0.21	0.23	0.23
Surface Energy (J/m ²)	3.91	3.24	3.43	3.38	3.53	3.61
Work Function (eV)	4.1	4.85	4.19	4.27	4.3	4.3

Table S6. The detailed energy of the $\text{CH}_3\text{O} \rightarrow \text{CH}_2\text{O}$ step. Calculated ground- and excited-state relative energies for the reaction step $\text{CH}_3\text{O}^* \rightarrow \text{CH}_2\text{O}^*$ on cluster models of WC surface (eV).

	$\text{CH}_3\text{O}^* \rightarrow \text{CH}_2\text{O}^*$	$\text{CH}_3\text{O}^* \rightarrow \text{CH}_2\text{O}^*$ (strained)
ground state	4.323	4.289
excited state 1	4.149	4.068
excited state 2	4.183	4.103
excited state 3	4.248	4.128
excited state 4	4.209	4.158

Table S7. Calculated interaction energies on cluster models of WC surface (eV) for CH₃OH and CO.

	WC	WC(strained)
CH ₃ OH	-0.7886	-0.5735
CO	-1.7711	-1.282

SI References

1. A. Kurlov, A. Gusev, Tungsten carbides and WC phase diagram. *Inorg. Mater* **42**, 121-127 (2006).
2. M. Miroshnichenko, V. Kolosov (2021) Production of tungsten carbide powder by the reaction of tungsten with ethanol. *J. Phys.: Conf. Ser.* **1942**, 012009.
3. S. D. Yim *et al.*, Decomposition of urea into NH₃ for the SCR process. *Ind. Eng. Chem. Res.* **43**, 4856-4863 (2004).
4. R. Liu *et al.*, W₂C nanorods with various amounts of vacancy defects: determination of catalytic active sites in the hydrodeoxygenation of benzofuran. *Catal. Sci. Technol.* **7**, 1333-1341 (2017).
5. J. Zhang *et al.*, A hydrogen-initiated chemical epitaxial growth strategy for in-plane heterostructured photocatalyst. *ACS Nano* **14**, 17505-17514 (2020).
6. Y. I. Jung, S. Y. Choi, S. J. L. Kang, Grain-growth behavior during stepwise sintering of barium titanate in hydrogen gas and air. *J. Am. Ceram. Soc.* **86**, 2228-2230 (2003).
7. K. M. Reddy *et al.*, Influence of heating rate on formation of nanostructured tungsten carbides during thermo-chemical processing. *Adv. Powder Technol.* **32**, 121-130 (2021).
8. Y. Duan *et al.*, Efficient sulfadiazine degradation via in-situ epitaxial grow of graphitic carbon nitride (g-C₃N₄) on carbon dots heterostructures under visible light irradiation: synthesis, mechanisms and toxicity evaluation. *J. Colloid Inter. Sci.* **561**, 696-707 (2020).
9. Y. J. Park, N. M. Hwang, D. Y. Yoon, Abnormal growth of faceted (WC) grains in a (Co) liquid matrix. *Metall. Mater. Trans. A* **27**, 2809-2819 (1996).
10. J. P. Palmquist *et al.*, Magnetron sputtered W-C films with C₆₀ as carbon source. *Thin Solid Film* **444**, 29-37 (2003).
11. J.-P. Palmquist, Z. Czigany, L. Hultman, U. Jansson, Epitaxial growth of tungsten carbide films using C₆₀ as carbon precursor. *J. Cryst. Growth.* **259**, 12-17 (2003).
12. M. Kato, H. Kawarada, Heteroepitaxial growth of tungsten carbide films on W (110) by plasma-enhanced chemical vapor deposition. *Jpn J. Appl. Phys.* **34**, 3628 (1995).
13. M. Bowker, Sustainable hydrogen production by the application of ambient temperature photocatalysis. *Green Chem.* **13**, 2235-2246 (2011).
14. M. Bowker, L. Millard, J. Greaves, D. James, J. Soares, Photocatalysis by Au nanoparticles: reforming of methanol. *Gold Bull.* **37**, 170-173 (2004).
15. M. Bowker *et al.*, Catalysis at the metal-support interface: exemplified by the photocatalytic reforming of methanol on Pd/TiO₂. *J. Catal.* **217**, 427-433 (2003).
16. A. Mills, M. Bingham, C. O'Rourke, M. Bowker, Modelled kinetics of the rate of hydrogen evolution as a function of metal catalyst loading in the photocatalysed reforming of methanol by Pt (or Pd)/TiO₂. *J. Photochem. Photobiol. A Chem.* **373**, 122-130 (2019).

17. X. Chen, D. Wu, P. Zhou, M. Chen, H. Yan, Modeling the solar absorption performance of Copper@ Carbon core–shell nanoparticles. *J. Mater. Sci.* 1-14 (2021).
18. S. Liang, X. Wang, L. Wang, W. Cao, Z. Fang, Fabrication of CuW pseudo alloy by W–CuO nanopowders. *J. Alloy. Compound.* **516**, 161-166 (2012).
19. Y. Li, C. Hou, H. Lu, S. Liang, X. Song, WC strengthened W–Cu nanocomposite powder synthesized by in-situ reactions. *Int. J. Refrac. Metal. Hard Mater.* **79**, 154-157 (2019).
20. Q. Gong *et al.*, Ultrasmall and phase-pure W₂C nanoparticles for efficient electrocatalytic and photoelectrochemical hydrogen evolution. *Nat. Commun.* **7**, 1-8 (2016).
21. Y. C. Kimmel, D. V. Esposito, R. W. Birkmire, J. G. Chen, Effect of surface carbon on the hydrogen evolution reactivity of tungsten carbide (WC) and Pt-modified WC electrocatalysts. *Int. J. Hydrogen Energy* **37**, 3019-3024 (2012).
22. S. B. Aziz, R. T. Abdulwahid, H. A. Rsaul, H. M. Ahmed, In situ synthesis of CuS nanoparticle with a distinguishable SPR peak in NIR region. *J. Mater. Sci. Mater. Electro.* **27**, 4163-4171 (2016).
23. S. Ruf, A. May, G. Emig, Anhydrous formaldehyde by sodium catalysis. *Appl. Catal. A Gen.* **213**, 203-215 (2001).
24. Z. Liu *et al.*, Room temperature stable CO_x-free H₂ production from methanol with magnesium oxide nanophotocatalysts. *Sci. Adv.* **2**, e1501425 (2016).
25. S. Gazi, M. Đokić, K. F. Chin, P. R. Ng, H. S. Soo, Visible light–driven cascade carbon–carbon bond scission for organic transformations and plastics recycling. *Adv. Sci.* **6**, 1902020 (2019).
26. Y. Chen *et al.*, Role of solvent rearrangement on Mg²⁺ solvation structures in dimethoxyethane solutions using multimodal NMR analysis. *J. Phys. Chem. Lett.* **11**, 6443-6449 (2020).
27. N. Uddin *et al.*, Zero-emission multivalORIZATION of light alcohols with self-separable pure H₂ fuel. *Appl. Catal. B Environ.* **292**, 120212 (2021).
28. M. Ahlawat, D. Mittal, V. Govind Rao, Plasmon-induced hot-hole generation and extraction at nano-heterointerfaces for photocatalysis. *Commun. Mater.* **2**, 1-15 (2021).
29. S. Linic, S. Chavez, R. Elias, Flow and extraction of energy and charge carriers in hybrid plasmonic nanostructures. *Nat. Mater.* 1-9 (2021).
30. S. Chavez, U. Aslam, S. Linic, Design principles for directing energy and energetic charge flow in multicomponent plasmonic nanostructures. *ACS Energy Lett.* **3**, 1590-1596 (2018).
31. S. Chavez, V. G. Rao, S. Linic, Unearthing the factors governing site specific rates of electronic excitations in multicomponent plasmonic systems and catalysts. *Faraday Discuss.* **214**, 441-453 (2019).
32. F. Dainton, I. Janovsky, G. Salmon, Evidence for the production of an oxidising radical on pulse-radiolysis of methanol. *J. Chem. Soc. D Chem. Commun.* 335-336 (1969).

33. Y. Yuan, Y. Iwasawa, Performance and characterization of supported rhenium oxide catalysts for selective oxidation of methanol to methylal. *J. Phys. Chem. B* **106**, 4441-4449 (2002).
34. W. Wang, R.-P. Ren, Y.-K. Lv, DFT study on the mechanism of methanol to methyl formate on the M@ C₁₆B₈ surface. *Mater. Today Commun.* **26**, 102090 (2021).
35. V. G. Rao, U. Aslam, S. Linic, Chemical requirement for extracting energetic charge carriers from plasmonic metal nanoparticles to perform electron-transfer reactions. *J. Am. Chem. Soc.* **141**, 643-647 (2018).
36. T. Chen, F. Tong, J. Enderlein, Z. Zheng, Plasmon-driven modulation of reaction pathways of individual Pt-modified Au nanorods. *Nano Lett.* **20**, 3326-3330 (2020).
37. Y. Kim, J. G. Smith, P. K. Jain, Harvesting multiple electron-hole pairs generated through plasmonic excitation of Au nanoparticles. *Nat. Chem.* **10**, 763-769 (2018).
38. F. Neese, Software update: the ORCA program system—version 5.0. *WIREs Comput. Mol. Sci.* **12**, e1606 (2022).
39. C. Bannwarth, S. Grimme, A simplified time-dependent density functional theory approach for electronic ultraviolet and circular dichroism spectra of very large molecules. *Comput. Theor. Chem.* **1040**, 45-53 (2014).
40. E. Berardo *et al.*, Describing excited state relaxation and localization in TiO₂ nanoparticles using TD-DFT. *J. Chem. Theory. Comput.* **10**, 5538-5548 (2014).
41. F. Weigend, R. Ahlrichs, Balanced basis sets of split valence, triple zeta valence and quadruple zeta valence quality for H to Rn: design and assessment of accuracy. *Phys. Chem. Chem. Phys.* **7**, 3297-3305 (2005).
42. D. Andrae, U. Haeussermann, M. Dolg, H. Stoll, H. Preuss, Energy-adjusted ab initio pseudopotentials for the second and third row transition elements. *Theor. Chim. Acta* **77**, 123-141 (1990).
43. Q. Zhang *et al.*, A robust electrocatalytic activity toward the hydrogen evolution reaction from W/W₂C heterostructured nanoparticles coated with a N, P dual-doped carbon layer. *Chem. Commun.* **55**, 9665-9668 (2019).
44. P. V. Krasovskii *et al.*, XPS study of surface chemistry of tungsten carbides nanopowders produced through DC thermal plasma/hydrogen annealing process. *Appl. Surf. Sci.* **339**, 46-54 (2015).
45. R. Tong, Z. Sun, X. Wang, S. Wang, H. Pan, Ultrafine WC_{1-x} nanocrystals: an efficient cocatalyst for the significant enhancement of photocatalytic hydrogen evolution on g-C₃N₄. *J. Phys. Chem. C* **123**, 26136-26144 (2019).
46. X. Fan, H. Zhou, X. Guo, WC nanocrystals grown on vertically aligned carbon nanotubes: an efficient and stable electrocatalyst for hydrogen evolution reaction. *ACS Nano* **9**, 5125-5134 (2015).

47. Z. Chen *et al.*, Eutectoid-structured WC/W₂C heterostructures: A new platform for long-term alkaline hydrogen evolution reaction at low overpotentials. *Nano Energy* **68**, 104335 (2020).
48. X. Xu *et al.*, Enriching hot electrons via NIR-photon-excited plasmon in WS₂@ Cu hybrids for full-spectrum solar hydrogen evolution. *Adv. Func. Mater.* **28**, 1804055 (2018).
49. M. C. Biesinger, Advanced analysis of copper X-ray photoelectron spectra. *Surf. Interface Anal.* **49**, 1325-1334 (2017).
50. S. Poulston, P. Parlett, P. Stone, M. Bowker, Surface oxidation and reduction of CuO and Cu₂O studied using XPS and XAES. *Surf. Interface Anal.* **24**, 811-820 (1996).
51. G. Schrauzer, T. Guth, Photolysis of water and photoreduction of nitrogen on titanium dioxide. *J. Am. Chem. Soc.* **99**, 7189-7193 (2002).
52. H. Liu *et al.*, Roles of Bi, M and VO₄ tetrahedron in photocatalytic properties of novel Bi⁰.₅M_{0.5}VO₄ (M= La, Eu, Sm and Y) solid solutions for overall water splitting. *J. Solid Stat. Chem.* **186**, 70-75 (2012).
53. Q. Wang *et al.*, Photocatalytic water splitting by band-gap engineering of solid solution Bi_{1-x}Dy_xVO₄ and Bi_{0.5}M_{0.5}VO₄ (M= La, Sm, Nd, Gd, Eu, Y). *J. Alloy. Compound.* **522**, 19-24 (2012).
54. W. J. Jo *et al.*, Phase transition-induced band edge engineering of BiVO₄ to split pure water under visible light. *Proc. Natl. Acad. Sci.* **112**, 13774-13778 (2015).
55. K. Yoshioka, V. Petrykin, M. Kakihana, H. Kato, A. Kudo, The relationship between photocatalytic activity and crystal structure in strontium tantalates. *J. Catal.* **232**, 102-107 (2005).
56. Z. Zou, J. Ye, K. Sayama, H. Arakawa, Direct splitting of water under visible light irradiation with an oxide semiconductor photocatalyst. *Nature* **414**, 625-627 (2001).
57. K. Sayama, H. Arakawa, K. Domen, Photocatalytic water splitting on nickel intercalated A₄Ta_xNb_{6-x}O₁₇ (A= K, Rb). *Catal. Today* **28**, 175-182 (1996).
58. D. W. Hwang, J. S. Lee, W. Li, S. H. Oh, Electronic band structure and photocatalytic activity of Ln₂Ti₂O₇ (Ln= La, Pr, Nd). *J. Phys. Chem. B* **107**, 4963-4970 (2003).
59. Y. Inoue, T. Niiyama, Y. Asai, K. Sato, Stable photocatalytic activity of BaTi₄O₉ combined with ruthenium oxide for decomposition of water. *J. Chem. Soc. Chem. Commun.* 579-580 (1992).
60. J. Luan *et al.*, Photophysical and photocatalytic properties of novel M₂BiNbO₇ (M= In and Ga). *J. Brazilian Chem. Soc.* **17**, 1368-1376 (2006).
61. J. Sato, N. Saito, H. Nishiyama, Y. Inoue, New photocatalyst group for water decomposition of RuO₂-loaded p-block metal (In, Sn, and Sb) oxides with d10 configuration. *J. Phys. Chem. B* **105**, 6061-6063 (2001).

62. C. Oshima *et al.*, Photocatalytic activity of ZnO/GaP_{1-x}N_x for water splitting. *J. Mater. Chem. A* **3**, 18083-18089 (2015).
63. X. Wang, K. Maeda, Y. Lee, K. Domen, Enhancement of photocatalytic activity of (Zn_{1-x}Ge_x)(N₂O_x) for visible-light-driven overall water splitting by calcination under nitrogen. *Chem. Phys. Lett.* **457**, 134-136 (2008).
64. K. Maeda, D. Lu, K. Domen, Direct water splitting into hydrogen and oxygen under visible light by using modified TaON photocatalysts with d⁰ electronic configuration. *Chem. A Euro. J.* **19**, 4986-4991 (2013).
65. J. Xu, C. Pan, T. Takata, K. Domen, Photocatalytic overall water splitting on the perovskite-type transition metal oxynitride CaTaO₂N under visible light irradiation. *Chem. Commun.* **51**, 7191-7194 (2015).
66. C. Pan *et al.*, A complex perovskite-type oxynitride: the first photocatalyst for water splitting operable at up to 600 nm. *Angew. Chem. Int. Ed.* **54**, 2955-2959 (2015).
67. C. Pan *et al.*, Band engineering of perovskite-type transition metal oxynitrides for photocatalytic overall water splitting. *J. Mater. Chem. A* **4**, 4544-4552 (2016).
68. G. Zhang, Z.-A. Lan, L. Lin, S. Lin, X. Wang, Overall water splitting by Pt/gC₃N₄ photocatalysts without using sacrificial agents. *Chem. Sci.* **7**, 3062-3066 (2016).
69. W. Liu *et al.*, Single-site active cobalt-based photocatalyst with a Long carrier lifetime for spontaneous overall water splitting. *Angew. Chem. Int. Ed.* **129**, 9440-9445 (2017).
70. Z. Wang *et al.*, Overall water splitting by Ta₃N₅ nanorod single crystals grown on the edges of KTaO₃ particles. *Nat. Catal.* **1**, 756-763 (2018).
71. L. Luo, P. A. Maggard, Effect of ligand coordination on the structures and visible-light photocatalytic activity of manganese vanadate hybrids. *Crystal Growth Des.* **13**, 5282-5288 (2013).
72. J. Luan *et al.*, Structural and photocatalytic properties of novel Bi₂GaVO₇. *Mater. Chem. Phys.* **104**, 119-124 (2007).
73. J. Luan *et al.*, Structural characterization and photocatalytic properties of novel Bi₂YVO₈. *Mater. Res. Bull.* **43**, 3332-3344 (2008).
74. H. Liu, J. Yuan, W. Shangguan, Y. Teraoka, Visible-light-responding BiYWO₆ solid solution for stoichiometric photocatalytic water splitting. *J. Phys. Chem. C* **112**, 8521-8523 (2008).
75. P. Dhanasekaran, N. Gupta, Factors affecting the production of H₂ by water splitting over a novel visible-light-driven photocatalyst GaFeO₃. *Int. J. Hydrogen Energy* **37**, 4897-4907 (2012).
76. G.-J. Lee, Y.-C. Zheng, J. J. Wu, Fabrication of hierarchical bismuth oxyhalides (BiOX, X= Cl, Br, I) materials and application of photocatalytic hydrogen production from water splitting. *Catal. Today* **307**, 197-204 (2018).

77. J. Yang *et al.*, Bi₂Ga₄O₉: An undoped single-phase photocatalyst for overall water splitting under visible light. *J. Catal.* **345**, 236-244 (2017).
78. B. Tian *et al.*, Supported black phosphorus nanosheets as hydrogen-evolving photocatalyst achieving 5.4% energy conversion efficiency at 353 K. *Nat. Commun.* **9**, 1-11 (2018).
79. L. Liao *et al.*, Efficient solar water-splitting using a nanocrystalline CoO photocatalyst. *Nat. Nanotechnol.* **9**, 69-73 (2014).
80. T. Takata *et al.*, Photocatalytic water splitting with a quantum efficiency of almost unity. *Nature* **581**, 411-414 (2020).
81. Q. Wang *et al.*, Scalable water splitting on particulate photocatalyst sheets with a solar-to-hydrogen energy conversion efficiency exceeding 1%. *Nat. Mater.* **15**, 611-615 (2016).
82. K. Watanabe, A. Iwase, A. Kudo, Solar water splitting over Rh_{0.5}Cr_{1.5}O₃-loaded AgTaO₃ of a valence-band-controlled metal oxide photocatalyst. *Chem. Sci.* **11**, 2330-2334 (2020).
83. Z. Ai *et al.*, Band-matching transformation between CdS and BCNNTs with tunable p-n homojunction for enhanced photocatalytic pure water splitting. *Nano Energy* **69**, 104408 (2020).
84. X. Cai *et al.*, Visible-light-driven water splitting by yolk-shelled ZnIn₂S₄-based heterostructure without noble-metal co-catalyst and sacrificial agent. *Appl. Catal. B Environ.* **297**, 120391 (2021).
85. M. Wang *et al.*, Red phosphorus/carbon nitride van der Waals heterostructure for photocatalytic pure water splitting under wide-spectrum light irradiation. *ACS Sust. Chem. Eng.* **8**, 13459-13466 (2020).
86. Z. Qin *et al.*, Synergistic effect of quantum confinement and site-selective doping in polymeric carbon nitride towards overall water splitting. *Appl. Catal. B Environ.* **261**, 118211 (2020).
87. X. Du *et al.*, BiVO₄@ZnIn₂S₄/Ti₃C₂ MXene quantum dots assembly all-solid-state direct Z-scheme photocatalysts for efficient visible-light-driven overall water splitting. *Appl. Mater. Today* **20**, 100719 (2020).
88. C. Zhao, M. Zheng, D. Wang, Q. Li, B. Jiang, Enhanced charge separation and transfer of Fe₂O₃@nitrogen-rich carbon nitride tubes for photocatalytic water splitting. *Energy Technol.* **8**, 2000108 (2020).
89. Y. Lin, W. Su, X. Wang, X. Fu, X. Wang, LaOCl-coupled polymeric carbon nitride for overall water splitting through a one-photon excitation pathway. *Angew. Chem. Int. Ed* **132**, 21105-21109 (2020).
90. Y. Dong *et al.*, Carbon quantum dots enriching molecular nickel polyoxometalate over CdS semiconductor for photocatalytic water splitting. *Appl. Catal. B Environ.* **293**, 120214 (2021).

91. W. Shi *et al.*, Facile synthesis of 2D/2D $\text{Co}_3(\text{PO}_4)_2/\text{g-C}_3\text{N}_4$ heterojunction for highly photocatalytic overall water splitting under visible light. *Chem. Eng. J.* **382**, 122960 (2020).
92. F. Liu *et al.*, Functionalized $\text{Cd}_{0.5}\text{Zn}_{0.5}\text{S}$ chalcogenide nanotwins enabling Z-scheme photocatalytic water splitting. *ACS Appl. Nano Mater.* **4**, 759-768 (2021).
93. Z. Qin *et al.*, Integrated Z-scheme nanosystem based on metal sulfide nanorods for efficient photocatalytic pure water splitting. *ChemSusChem* **13**, 6528-6533 (2020).
94. W. Fu, X. Guan, Y. Si, M. Liu, Phosphatized GaZnInON nanocrystals with core-shell structures for efficient and stable pure water splitting via four-electron photocatalysis. *Chem. Eng. J.* **410**, 128391 (2021).
95. W. Cui, L. Feng, C. Xu, S. Lü, F. Qiu, Hydrogen production by photocatalytic decomposition of methanol gas on Pt/TiO_2 nano-film. *Catal. Commun.* **5**, 533-536 (2004).
96. G. Halasi, G. Schubert, F. Solymosi, Comparative study on the photocatalytic decomposition of methanol on TiO_2 modified by N and promoted by metals. *J. Catal.* **294**, 199-206 (2012).
97. A. Gazsi, G. Schubert, T. Bánsági, F. Solymosi, Photocatalytic decompositions of methanol and ethanol on Au supported by pure or N-doped TiO_2 . *J. Photochem. Photobiol. A Chem.* **271**, 45-55 (2013).
98. C.-H. Lin, J.-H. Chao, W.-J. Tsai, M.-J. He, T.-J. Chiang, Effects of electron charge density and particle size of alkali metal titanate nanotube-supported Pt photocatalysts on production of H_2 from neat alcohol. *Phys. Chem. Chem. Phys.* **16**, 23743-23753 (2014).
99. Y. Pang *et al.*, Colloidal single-layer photocatalysts for methanol-storable solar H_2 fuel. *Adv. Mater.* **31**, 1905540 (2019).
101. W. Cui *et al.*, Hydrogen evolution by photocatalysis of methanol vapor over Ti-beta. *J. Photochem. Photobiol. A Chem.* **175**, 89-93 (2005).
102. Y. Liu *et al.*, In situ construction of fibrous $\text{AgNPs/g-C}_3\text{N}_4$ aerogel toward light-driven CO_x -free methanol dehydrogenation at room temperature. *Chem. Eng. J.* **334**, 2401-2407 (2018).